J. Fluid Mech. (2001), *vol.* 431, *pp.* 189–222. Printed in the United Kingdom

Planar velocity measurements in compressible mixing layers

By WILLIAM D. URBAN AND M. G. MUNGAL

Department of Mechanical Engineering, Stanford University, Stanford, CA 94305, USA

(Received 30 August 1999 and in revised form 17 July 2000)

In the present study, we use particle image velocimetry (PIV) to obtain planar, two-component velocity fields in two-dimensional, turbulent mixing layers at convective Mach numbers M_c of 0.25, 0.63, and 0.76. The experiments are performed in a large-scale blowdown wind tunnel, with high-speed free-stream Mach numbers up to 2.25 and shear-layer Reynolds numbers up to 10^6. Specific issues relating to the application of PIV to supersonic flows are addressed. The instantaneous data are analysed to produce maps of derived quantities such as vorticity, and ensemble averaged to provide turbulence statistics. The results show that compressibility introduces marked changes in the disposition of instantaneous velocity gradients within the layer, and hence in the vorticity field. In particular, peak transverse vorticity values are seen to be confined to thin streamwise sheets under compressible conditions, with little transverse communication. The location of these sheets near the lab-frame sonic velocity suggests a sensitivity of the compressible layer to stationary disturbances. Turbulence statistics derived from the planar velocity measurements confirm previous observations of strong suppression of transverse velocity fluctuations and primary Reynolds stress as M_c increases between 0.25 and 0.76.

1. Introduction

1.1. *Background and flow description*

In this work, we are concerned with compressible mixing, that is, mixing between gaseous flows under conditions where Mach number effects are important. The principal practical application for this class of flows is in the mixing of fuel and air in high-Mach-number air-breathing propulsion devices.

Figure 1 depicts key features of the flow which will arise continually throughout this work. The two principal, uniform flows are initially separated by a splitter plate. The high- and low-speed streams are labelled 1 and 2; the arrangement with flow from left to right and the high-speed stream on top reflects the layout of our experiment, and is used throughout this work. The plate tapers to a tip, downstream of which the two flows interact and form a turbulent mixing region whose lateral extent grows along the streamwise coordinate. After an initial, nonlinear growth region, the layer reaches a self-similar state where subsequent growth is linear with downstream distance. A Cartesian coordinate system with its origin at mid-span of the tip of the splitter plate defines the streamwise direction x, the transverse direction y and the spanwise direction z. Extrapolation of the asymptotic growth rate to zero thickness defines the location of a virtual origin x_0, y_0. A general symbol for the mixing layer thickness is δ, whose definition may arise from consideration of profiles of velocity, vorticity, total pressure, or scalar concentration, or from various side-view visualizations of the layer.

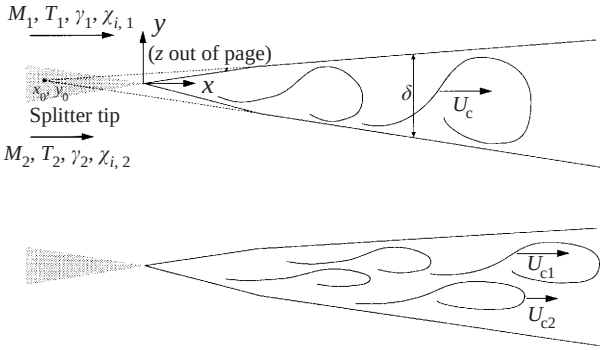

FIGURE 1. Mixing layer schematic. Incompressible view (*a*) features a single family of large-scale structure arising from primary instability and characterized by convective velocity U_c. Co-layer concept (*b*) permits the growth of multiple instabilities, leading to separate families of structures.

In the present work, we will rely largely on b, the 90% thickness of the mean velocity profile. Since the approach of the velocity profile to the free stream is relatively slow, b is considerably smaller than the visual or scalar thicknesses often used in other work. In practice, b is seen to be approximately equal (Goebel & Dutton 1990) to the vorticity thickness δ_ω. The vorticity thickness, in turn, is equal to about half the visual thickness δ_{vis} (Brown & Roshko 1974).

Although the free-stream conditions are adjusted so that the mixing layer departs horizontally from the splitter tip, asymmetric growth leads to a depression of the centreline of the layer in the far field. Therefore, normalization of the transverse coordinate is conducted relative to the local layer centreline y_{cl}, defined as the point where $\bar{u} = 0.5(U_1 + U_2)$, rather than $y = 0$. This leads to the coordinate $\eta \equiv (y - y_{\text{cl}})/b$.

1.2. *Literature survey*

We present here the context of previous work which provided sources of motivation, guidance, and comparison for the present work.

1.2.1. *Theoretical and analytical foundations*

The establishment of growth-rate models has long been a central objective in the analytical study of mixing layers. The constant-density result of Abramowich (1963) and Sabin (1965), while adequate for incompressible layers, is unable to predict the strong growth-rate suppression in supersonic shear layers (Birch & Eggers 1972). Correction of the growth-rate relation with a density-ratio effect in jet experiments is obstructed by the difficulty of decoupling the density and velocity ratios from one another and from their streamwise evolution. Brown (1974) overcame this problem by working with a planar shear layer composed of dissimilar gases, allowing him to derive and verify a more sophisticated growth-rate relation. Furthermore, the discovery by Brown & Roshko (1974) of unambiguous large-scale structures convecting within the mixing layer underpinned the convective-frame theoretical foundations of this result. Also, Brown & Roshko (1974) observed significant differences between their zero-Mach-number growth-rate results and those of supersonic studies (e.g. Ikawa 1973) at comparable density ratios and $r = 0$, leading them to conclude that an additional compressibility effect remained to be isolated.

Toward this end, Bogdanoff (1983) proposed a Mach number M^+ based on the velocity U_c of the large-scale structures relative to either free stream. This result was recast and supported experimentally by Papamoschou & Roshko (1988), who defined

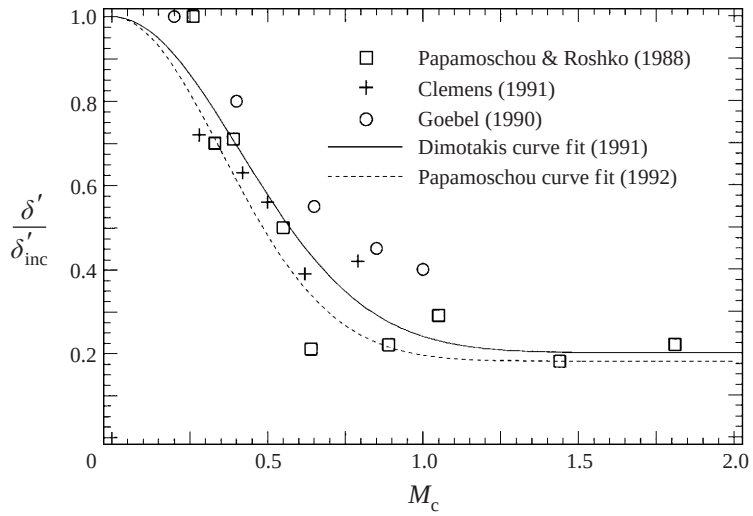

FIGURE 2. Growth-rate suppression.

a *convective Mach number* for each stream:

$$M_{c_1} \equiv \frac{U_1 - U_c}{a_1}, \tag{1.1}$$

$$M_{c_2} \equiv \frac{U_c - U_2}{a_2}. \tag{1.2}$$

In general, this analysis leads to an implicit system for U_c, M_{c_1}, and M_{c_2}. However, for $\gamma_1 = \gamma_2$, an explicit result is available:

$$U_c = \frac{a_2 U_1 + a_1 U_2}{a_1 + a_2}, \tag{1.3}$$

$$M_{c_1} = M_{c_2} = \frac{U_1 - U_2}{a_1 + a_2}. \tag{1.4}$$

For the present work, the free-stream values of γ differ only in the $M_c = 0.76$ case; here, (1.4) returns a result within 1% of the mean of M_{c_1} and M_{c_2}, which themselves only differ by 9%. Therefore, the 'average' value of M_c given by (1.4) will be used in all cases.

To quantify the M_c dependence for compressible layers, it has become customary to break the three-variable dependence $d\delta/dx = f(r, s, M_c)$, where r is the velocity ratio U_2/U_1 and s the density ratio ρ_2/ρ_1 into two relations; the growth rate of the analogous incompressible layer (i.e. same r and s) is corrected for compressibility by a relation giving $(d\delta/dx)/(d\delta/dx)_{inc} = f(M_c)$. This second relation (figure 2) may be derived from a curve fit to experimental data (Dimotakis 1991; Papamoschou 1992), or extracted from numerical analysis (Vreman, Sandham & Luo 1996). The half-Gaussian of Dimotakis (1991) is a good fit to the experimental data in figure 2:

$$\frac{(d\delta/dx)}{(d\delta/dx)_{inc}} = 0.8e^{-3M_c^2} + 0.20. \tag{1.5}$$

Because numerous measured values of U_c have shown strong departures from (1.3), the theoretical footing of M_c has been challenged; indeed, some workers (e.g. Goebel

& Dutton 1991) prefer to use the *relative Mach number* $M_r \equiv 2\Delta U/(a_1 + a_2)$ instead. However, the widespread use of M_c compels us to retain it as our compressibility parameter. It should further be noted that M_c derivations do not necessarily rely upon (1.3) or the postulation of isentropic deceleration of free-stream fluid. Most linearized stability analyses derive M_c from consideration of the travelling speed of the most-amplified disturbances, while that of Jackson & Grosch (1990) is rooted in the lab frame and is independent of either U_c or any wave speed.

Although the early stages of entrainment ('engulfment') are dominated by the largest scales (Dimotakis & Brown 1976), the impairment of layer growth by compressibility suggests some alteration of this fact under supersonic conditions. A scaling rule for compressible turbulence was supplied by Breidenthal (1992), who argued that the characteristic velocity of an eddy must at most be sonic for effective entrainment; therefore, he proposed an upper limit λ^* on entraining eddy size based upon the global velocity gradient of the layer:

$$\frac{\lambda^*}{\delta} = \frac{a^*}{\Delta U} \approx \frac{1}{2M_c}. \tag{1.6}$$

This model inspires us to look for confinement of vortical structure to a region within the layer boundaries, rather than spanning its full extent; for our compressible cases, λ^*/δ is approximately 0.7.

1.2.2. *Numerical modelling*

Several stability analyses of the compressible shear layer (e.g. Ragab & Wu 1989) have substantiated the convective Mach number as a compressibility parameter, while others (Lessen, Fox & Zien 1966; Gropengiesser 1969) have introduced instability modes biased toward the free streams, an idea developed further by Jackson & Grosch (1989). More recently, the nature of these 'outer modes' and their interplay with the central mode was parametrized in detail by Day, Reynolds & Mansour (1998). They characterized the conditions of compressibility, density ratio, and heat release under which one or more outer modes are likely to become significant. For the non-reacting layer at density ratios near 1, they indicated a transition from two- to three-dimensional central modes near $M_c = 0.6$, with the appearance of outer modes not likely until M_c of at least 2.

Simulations of the compressible mixing layer have steadily increased in sophistication with improvements in computational resources. Although they differ in approach, all of these studies have sought to confirm and explain experimental observations regarding the changes in structural and field characteristics brought on by compressibility. Early work featured two- and three-dimensional inviscid calculations (Soetrisno *et al.* 1989; Leep, Dutton & Burr 1993) and two-dimensional direct simulations (Lele 1989; Ragab & Sheen 1990). Papamoschou & Lele (1993) simulated the two-dimensional interaction of an Oseen vortex with the compressible shear layer, and documented suppression of pressure variation and induced velocity with increasing compressibility. These reductions in spatial communication suggest a decrease in the ability of the eddy motion to concertedly entrain and mix fluid, leading to growth-rate reduction. Recently, a three-dimensional direct simulation by Freund (1997) examined the circular shear layer in the early development of a supersonic jet, providing detailed information about field and turbulence quantities in compressible turbulence. A key difference between the early, two-dimensional simulations and newer work (e.g. Vreman *et al.* 1996) is that significant eddy shocklets are predicted at relatively

low compressibility levels only when three-dimensional effects are omitted from the simulation.

1.2.3. *Structural observations and growth-rate measurements*

The success of the work of Brown & Roshko (1974) in addressing growth rate and large-scale structure in incompressible mixing layers made these issues the natural starting point for compressible studies. The experiments summarized in Birch & Eggers (1972) documented growth-rate suppression in supersonic jets, but the corresponding result for two-stream mixing layers did not appear until the work of Chinzei *et al.* (1986). Shortly afterward, Papamoschou & Roshko (1988) published a more comprehensive study, covering a wide parameter space, providing extensive interpretation, and deriving the convective Mach number as described above. Using various combinations of gases and free-stream Mach numbers, the authors obtained schlieren and Pitot pressure data over the range $0.07 \leqslant M_c \leqslant 1.81$. The schlieren photographs display large-scale structure, particularly at lower compressibilities, while the growth rates inferred from the Pitot profiles substantiated the growth-rate suppression with compressibility. The ten cases studied in the paper permitted the authors to characterize the normalized growth-rate curve thoroughly, with its rapid drop from $(\mathrm{d}\delta/\mathrm{d}x)/(\mathrm{d}\delta/\mathrm{d}x)_{\mathrm{inc}} = 1$ between $M_c = 0$ and $M_c = 0.5$, and its subsequent saturation near $(\mathrm{d}\delta/\mathrm{d}x)/(\mathrm{d}\delta/\mathrm{d}x)_{\mathrm{inc}} = 0.2$ as M_c approaches unity (figure 2). Clemens & Mungal (1995) documented the degeneration of large-scale structure with increasing M_c, whereby the two-dimensional 'rollers' of the incompressible case give way to the diffuse, disorganized compressible layer. A large body of additional work devoted to motion analysis of large-scale structures is summarized in Urban (1999).

1.2.4. *Velocity measurements*

Although early studies used Pitot probe measurements to determine shear-layer thickness (e.g. Papamoschou & Roshko 1988), and some investigators (e.g. Barre, Quine & Dussauge 1994 and Bowersox & Schetz 1995) have applied hot-wire techniques, detailed velocity surveys of compressible mixing layers have largely depended upon non-intrusive laser diagnostics. The superiority of optical methods is particularly evident in compressible flows, where flow disturbances due to intrusive probes are especially severe, environments are often hostile, and dynamic-pressure loading is high. Furthermore, the large gas appetites of supersonic flow facilities often force workers to work at small physical scales, where resolution limitations of probes also become a severe handicap.

Two exhaustive studies (Elliott & Samimy 1990; Goebel & Dutton 1991) applied two-component laser-Doppler velocimetry (LDV) to the compressible shear layer, providing pointwise measurements of mean kinematic quantities and turbulence statistics. Collectively, these studies covered a compressibility range from $M_c = 0.20$ to $M_c = 0.99$, a total of eight experimental conditions. Both studies were carried out in blowdown wind tunnels similar to the present facility. Elliott & Samimy (1990) used atomized silicone oil droplets as the flow tracer, while Goebel & Dutton (1991) employed a TiO_2 fluidized bed similar to the one used here. Both studies concluded that the transverse turbulence intensity σ_v and the primary Reynolds stress $\langle u'v' \rangle$ experience strong attenuation with increasing compressibility. However, Goebel & Dutton (1991) reported no significant alteration in the streamwise turbulence intensity σ_u, while Elliott & Samimy (1990) observed a decrease similar to that in the other statistics. Although the final conclusions of the authors differ in this way, the discrepancy is at least partially obscured by the differences in experimental conditions

between the studies. Elliott & Samimy (1990) examined conditions at $M_c = 0.51$, 0.64, and 0.86; over this range, σ_u decreased less than 20%. Additional depression in σ_u is implied by their plotted comparison with the incompressible result of Oster & Wygnanski (1982). Goebel & Dutton (1991), on the other hand, showed a reduction of about 25% between their measurements at $M_c = 0.2$ and $M_c = 0.46$, but changing very little thereafter. However, the authors warn that the incompressible result lacked self-similar profiles of turbulence quantities, suggesting incomplete development in the form of a residual wake component. In summary, both studies do show some effect of compressibility on σ_u, but the decreasing trend is clearer in the work of Elliott & Samimy (1990).

The extension of LDV to three components in this flow was performed by Gruber, Messersmith & Dutton 1993, who obtained all velocity perturbations as well as turbulent kinetic energy measurements at a single compressibility ($M_c = 0.80$). They found that the spanwise and streamwise turbulence intensities were unaltered relative to previous incompressible measurements, while the primary Reynolds stress and turbulence kinetic energy were suppressed. From the resulting decrease in y, z normal stress anisotropy σ_v/σ_w, they inferred that three-dimensional turbulence plays an enhanced role in compressible layers, paralleling the increased importance of three-dimensional structure. Several other LDV studies provide support to these results. Chang *et al.* (1993) presented brief results for a transonic, yet incompressible, reacting layer; while Debisschop, Chambres & Bonnet (1994) provided measurements at moderate to high compressibility levels.

The effectiveness of PIV in high-speed flows had already been demonstrated by several workers; cases considered include jets (Kompenhans & Höcker 1988; Bryanston-Cross & Epstein 1990; Ross 1993, Krothapalli, Wishart & Lourenço 1994; Strykowski, Krothapalli & Forliti 1996), wakes (Molezzi & Dutton 1993), boundary layers (Glawe *et al.* 1996), and external flows (Crisler, Krothapalli & Lourenço 1994; Raffel *et al.* 1996). On the other hand, velocity surveys of the compressible mixing layer using advanced planar techniques have been extremely limited. A proof-of-concept study (Elliott, Samimy & Arnette 1994) demonstrated the use of planar Doppler velocimetry (PDV), providing planar maps of one velocity component and reproducing mean-velocity profiles. Using particle image velocimetry (PIV), the present programme has delivered two-component planar measurements (Urban & Mungal 1997*b*), combined them with structure velocimetry results (Urban & Mungal 1997*a*), and examined a range of compressibilities (Urban, Watanabe & Mungal 1998; Urban & Mungal 1998). A PIV study at low levels of compressibility was recently presented by Olsen (1999).

2. Experimental apparatus and conditions

2.1. *Flow facility*

The planar shear layer is generated using a two-stream, blowdown wind tunnel (figure 3) designed and previously used for both non-reacting (Clemens 1991; Island 1997) and reacting (Miller 1994) experiments. By varying the chemical compositions, Mach numbers, and temperatures of the two streams, a wide variety of mixing-layer conditions may be achieved. All experiments in the present study are non-reacting cases in which the free-stream gases are either air or argon, expanded from ambient stagnation temperature.

The wind tunnel consists of separate settling chambers, contractions and nozzles

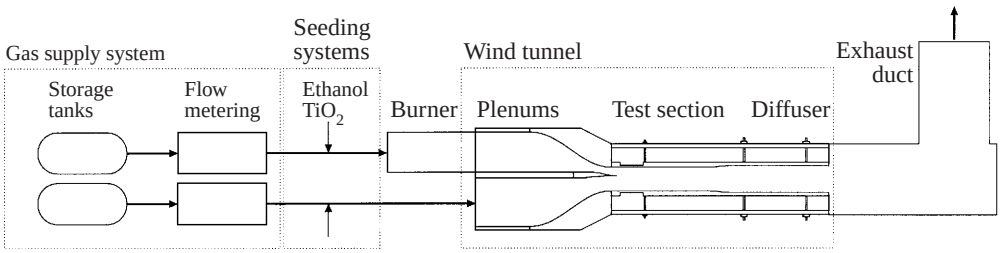

FIGURE 3. Flow facility.

for each stream, a test section where the mixing between the streams takes place, and a diffuser. Extensive use is made of cooled copper construction to permit operation at high stagnation temperatures.

The test section is 10 cm wide in the spanwise (z) direction, 8 cm high in the transverse (y) direction, and 48 cm long in the streamwise (x) direction. Two sets of upper and lower test section walls are provided: the outer walls provide a gas-tight seal to the room and a structural connection to the sidewalls, which are continuous from the plenums through the diffuser. The inner walls bound the flow channel in the transverse direction and are adjustable in order to control the streamwise pressure gradient. For the $M_c = 0.63$ and $M_c = 0.76$ cases, each wall is converged by 0.5° in order to eliminate the gradient; at $M_c = 0.25$, each wall is diverged by 0.25° to minimize compressibility. The divergence has the effect of accelerating both streams and reducing the overall shear (Clemens 1991; Island 1997). Typical absolute test section pressures are 60–80 KPa.

2.2. *PIV apparatus*

2.2.1. *Seeding system*

In order to obtain reasonable seeder size and final particle mass loading, only a fraction (approximately 1%) of each free-stream flow (the *carrier gas*) is routed through the seeders. Each seeder consists of a fluidized bed contained in a pressure vessel (Ross 1993; Crosswy 1985; Patrick 1985). Carrier gas is admitted through a multi-holed injector at the bottom of the chamber, and proceeds through a 10–25 cm bed of seed, which becomes fluidized at the design operating condition. At the top of the seeder, the particle-laden flow leaves through a tortuous exit baffle. The agglomeration typical with solid seed particles is reduced through the use of hydrodynamic seed-conditioning elements. In the low-speed stream, a cyclone separator (Patrick 1985; Nichols 1985) is used, while the high-speed stream uses a hybrid cyclone-impactor design.

2.2.2. *Seed particle selection and performance*

The suitability of a seeding strategy for a particular application is a composite of the ability of the seed to follow the flow and the ability of the imaging and analysis system to record and analyse a field of particle images. Our initial selection of candidate tracer particles focused on monodispersity, pressure and temperature envelope, health hazard, and cost; in the discussion that follows, we present the evaluation of particle dynamics that drove our final selection.

Consideration of seed-particle dynamics is especially important for PIV measurements in high-speed flows, since large velocity gradients challenge the flow-following capability of all but the smallest particles, and spatial variations in density make it

difficult to establish uniformly satisfactory seeding levels. Additionally, particles lagging high-speed vortical flows will be expelled from the vortices, forming preferential concentration patterns apart from the fluid density field (Glawe & Samimy 1993; Wang & Squires 1996). As has been observed for LDV (Samimy & Abu-Hijleh 1989), as well as for PIV (Urban 1999), the statistical distribution of particle sizes can couple with the sensitivity of the imaging system to introduce still further effects. Finally, we note that conditions for particle lag are dependent not only on the particles and the integral-scale behaviour of the fluid but also on the relationship between spatial variations in fluid velocity and the resolution of the imaging system. Raffel *et al.* (1996) noted that the particles need only track the velocity variations from one PIV interrogation region to another, and that velocities along gradients too steep for the particles to follow will nevertheless be reflected faithfully in the average values reported for their interrogation regions. For the present experiment, however, we have still attempted to optimize particle performance to ensure that our spatial resolution is sensor-limited rather than particle-limited.

In the seed performance experiments described below 0.3 μm alumina (Al_2O_3) particles from Praxair and the 0.015 μm titanium dioxide (TiO_2) particles from Tioxide were used. It should be noted that the manufacturers' nominal sizing for both products is somewhat misleading. The alumina particles are actually fairly widely dispersed (Crosswy 1985), and readily agglomerate into larger clumps. In the case of the TiO_2, the 15 nm figure refers to a 'fundamental' particle size, with actual samples consisting of indivisible agglomerates approximately ten times larger. The fundamental particle size serves mainly to distinguish this product, an 'ultra-fine' grade, from the pigment-grade 0.23 μm-nominal material, which in practice agglomerates to yet larger sizes. For particles in this size range, a rule of thumb is that agglomeration increases the effective particle size by about an order of magnitude. Therefore, to achieve the submicron sizes desired in the test section, it was necessary to specify the ultra-fine powder.

Particle dynamic effects are normally parametrized by the Stokes number St, the ratio of characteristic particle time τ_p to the time scale τ_f of the flow variations to be measured. For effective flow-following at the scale represented by τ_f, we require that $St \ll 1$. The particle time is the $1/e$ time constant for a particle to react to a step input in relative velocity. In the present case (low relative Mach and Reynolds numbers, but very small particles), the drag relation of Melling (1986) is adequate to determine the particle time:

$$C_D = \frac{24}{Re_d(1 + 2.7Kn_d)} \tag{2.1}$$

where Re_d is the Reynolds number and Kn_d the Knudsen number, both based on particle diameter, which leads to

$$\tau_p = \frac{\rho_p d_p^2}{18\mu}(1 + 2.7Kn_d) \tag{2.2}$$

where ρ_p is particle material density and μ is dynamic viscosity.

For the present experiment, the integral-scale fluid-mechanical time, given by $\delta/\Delta U$, is approximately 60 μs. Therefore, for satisfactory flow-following we seek a particle with τ_p below 10 μs. Applying (2.2) to the manufacturers' claimed properties of our candidate particles, we arrive at unrealistically low τ_p estimates of 2.3 μs for the Al_2O_3 and 8.2 ns for the TiO_2. Clearly, it is necessary to measure τ_p, to infer an effective particle diameter from it, and in turn to use this to identify and characterize

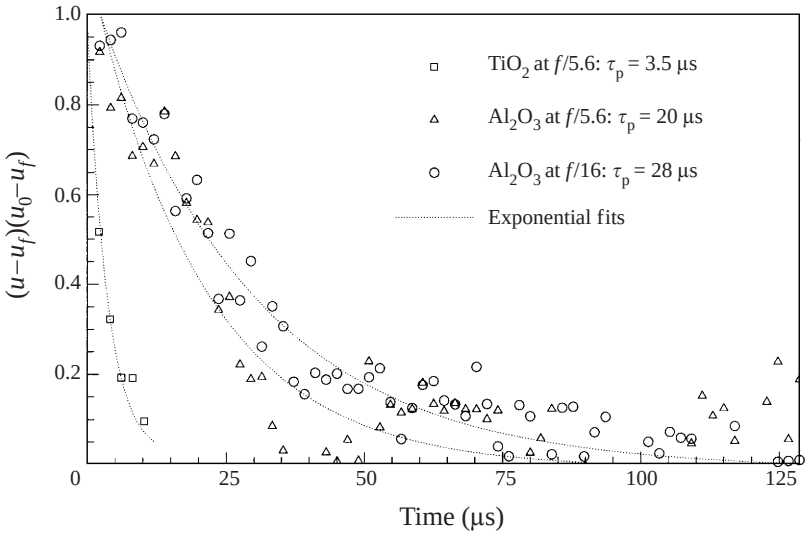

FIGURE 4. Particle relaxation traces.

an acceptable seed. The strong influence of particle diameter on particle dynamics suggested by (2.2) motivates us to make this measurement in our test section, under conditions similar to those in our mixing-layer experiments.

Seed particle performance is assessed through measurements of particle lag downstream of a two-dimensional oblique shock, with changes in the seed particles and the optical arrangement leading to estimates of the magnitude and variability of particle dynamic effects. The high-speed stream of the mixing layer facility is used to provide a supersonic ($M = 1.8$) approach flow, and an oblique shock is generated by a two-dimensional 10° wedge mounted on the top wall of the tunnel.

Analysis of the wedge-flow particle images leads to measurements of cross-shock velocity profiles for the two seeds (figure 4). By transforming the spatial coordinate to time and applying exponential fits, we estimate τ_p to be 20–28 μs for the Al_2O_3 seed and 3.5 μs for the TiO_2 seed, translating to effective diameters of 1.2 and 0.4 μm respectively. These measurements agree well with the scattering-based measurements of Crosswy (1985). In summary, the TiO_2 seed ($St \approx 0.06$) best satisfies our specifications with regard to particle dynamic performance, cost, and ease of handling, so it is chosen for the mixing-layer measurements.

2.2.3. *PIV imaging and analysis system*

The PIV system is shown in figure 5. The plane of interest is illuminated by a Nd:YAG laser (Spectra-Physics PIV-400) containing two independent cavities, permitting the generation of pulse pairs with arbitrary time separation. Output from the two cavities is polarization combined before proceeding through a common frequency-doubling crystal, resulting in collinear beams at energies up to 400 mJ per laser per 8 ns pulse at 532 nm. The nominal repetition rate is 2 Hz, although in practice the laser is triggered at rates between 0.6 and 3.2 Hz in order to synchronize with the imaging hardware. Within this range, the thermal balance in the pumping chambers is sufficiently stable that deterioration of beam quality or pulse energy due to thermal lensing was not encountered. Timing of the laser pulses, as determined by the flashlamp and Q-switch of each of the two cavities, is effected by a four-channel digital delay generator (Stanford Research Systems DG535).

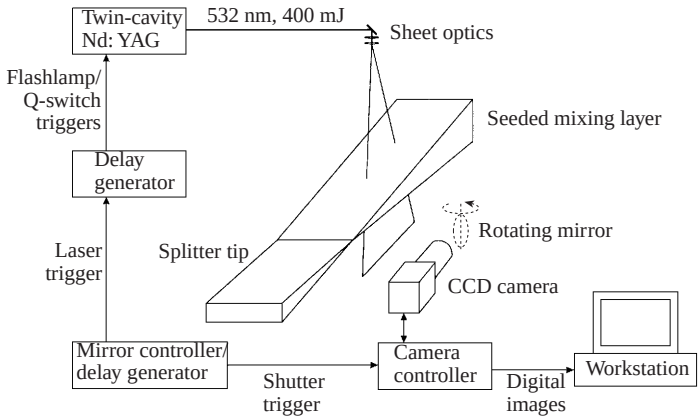

FIGURE 5. PIV system (side-view configuration).

Double-exposed particle images of the region of interest are acquired at 90° by a slow-scan, unintensified CCD camera (Kodak Megaplus 4.2) featuring a high-resolution detector containing 2000×2000 9 μm pixels. The imaging lens is a 200 mm focal length macro lens (Nikon) with a maximum aperture of $f/4.5$, typically set to $f/16$ in order to optimize particle image size and depth of field. In order to improve signal levels and minimize consumption of seed particles, a gain of +12 dB is applied at the A/D converter in the camera controller.

For the compressible ($M_c = 0.63$ and $M_c = 0.76$) PIV measurements, a rotating mirror (FFD, Inc.) is placed in the imaging train to enlarge the particle image displacements, permitting shorter values of Δt.

The double-exposed particle images are processed to yield velocity fields via a two-step process. First, raw particle-image displacement fields are calculated by means of FFT-based autocorrelations using commercial PIV software (TSI, Inc. MKIV/Insight). Subsequently, the velocity fields are analysed by custom software to exert precise control over validation, interpolation, averaging, and the extraction of derived quantities. Note that directional ambiguity, frequently cited as a drawback of the autocorrelation technique, is readily resolved in the present flow; the half-plane in which all velocity vectors reside may be readily assigned *a priori*, since there are no flow reversals in the lab frame.

2.3. *Experimental conditions*

All experiments described in this dissertation are conducted at one of the three flow conditions summarized in table 1. These conditions approximate as closely as possible the $M_c = 0.25$, $M_c = 0.63$, and $M_c = 0.76$ conditions of Island (1997), in order to facilitate comparison with that work. The $M_c = 0.76$ case is attained through the use of argon in the low-speed free stream, resulting in increased shear and therefore compressibility.

2.3.1. *Pressure profiles*

Average streamwise static pressure profiles from the top and bottom walls of the wind tunnel for the three cases investigated in § 3 are presented in figure 6. At $M_c = 0.25$, the acceleration due to the diverged test section walls is evident in the gradual pressure decrease throughout the test section. In all cases, pressure

Case	$M_c = 0.25$		$M_c = 0.63$		$M_c = 0.76$	
Stream	1	2	1	2	1	2
Bulk gas	Air	Air	Air	Air	Air	Argon
M_{ex}	1.48	0.80	2.18	0.51	2.17	0.37
δ_{99} (mm)	1.6	1.0–1.5	1.6	1.0–1.5	1.6	1.0–1.5
θ (mm)	0.15	—	0.12	—	0.12	—
$\dot{m}$ (kg s^{-1})	1.4	1.2	2.1	0.72	1.7	0.57
M_{img}	1.64	0.97	2.22	0.54	2.17	0.37
U_{img} (m s^{-1})	441	296	525	175	522	111
T_{img} (K)	176	227	136	255	139	258
P_{img} (kPa)	64	65	67	70	58	58
$r \equiv U_2/U_1$	0.67		0.33		0.21	
$s \equiv \rho_2/\rho_1$	0.77		0.53		0.77	
x_{img} (cm)	38		24		24	
U_c (m s^{-1})	374		377		342	
δ_{vis} (cm)	1.8		2.5		2.5	
$Re_\delta/1000$	150		400		1000	
$Rx/30\theta$	10		20		60	

TABLE 1. Experiment conditions: M_{ex} is the nozzle exit Mach number, δ_{99} the boundary layer 99% velocity thickness, θ the boundary layer momentum thickness, $\dot{m}$ the mass flow rate, δ_{vis} mixing layer visual thickness, Re_θ Reynolds number based on momentum thickness, $Rx/30\theta$ mixing layer pairing parameter, and subscript 'img' denotes quantities measured at the imaging station.

fluctuations resulting from stationary waves in the high-speed stream appear in the top-wall pressure profiles.

2.3.2. *Schlieren*

Representative instantaneous Toepler schlieren images for the $M_c = 0.25$ and $M_c = 0.63$ cases (figure 7) provide an overview of the flow field. Flow is from left to right, and the high-speed stream is at the top. These visualizations highlight the change in mixing layer structure as compressibility is increased: the spanwise-coherent 'roller' structures at low compressibility give way to a more disorganized, diffuse appearance at high compressibility. This result is confirmed by planar scalar images (e.g. Clemens 1991), which are not spanwise-integrated. The schlieren images also serve to show up several differences between the idealized planar shear layer of figure 1 and that generated in the laboratory. First, we see that the experimental flow is confined, and indeed that the channel walls are close enough to affect the shear layer growth at downstream locations. Next, we note the presence of boundary layers not only on the walls but also on both sides of the splitter tip, as well as the finite thickness of the latter; this introduces a wake component to the flow in the early developing region. Finally, the supersonic stream contains an extensive array of wave disturbances. The primary sources are separation of the high-speed boundary layer on the upper splitter tip, mismatch between the contraction and top wall (immediately above the splitter tip), and window-wall mismatches in the top wall (at arrows near $x = 15$ cm). Reflections of these waves between the top wall and the mixing layer give rise to the cross-hatched pattern visible in the figure. The pressure measurements described above attest to the weakness of the waves in this system.

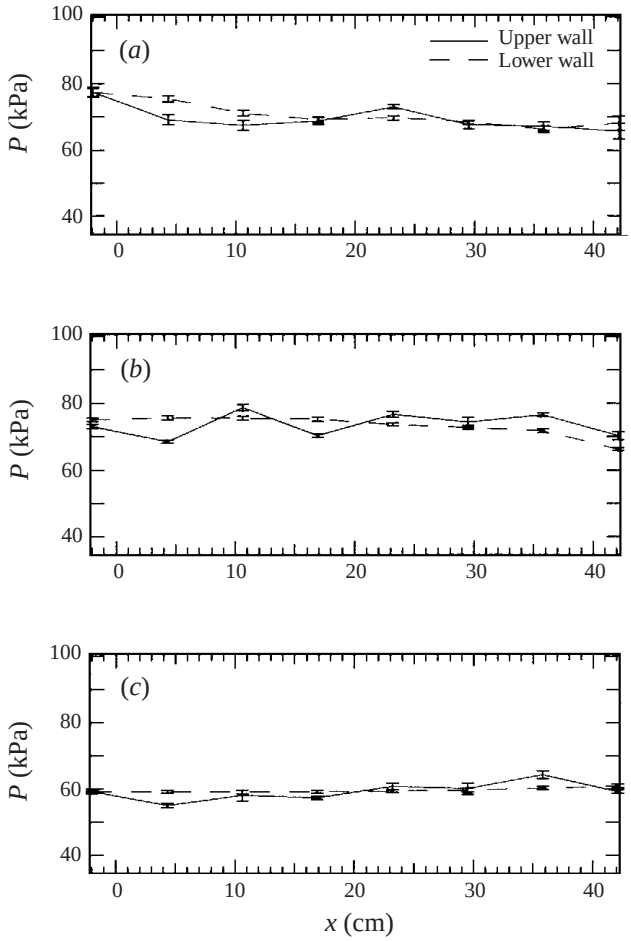

FIGURE 6. Static pressure profiles for $M_c = 0.25$ (*a*), $M_c = 0.63$ (*b*), and $M_c = 0.76$ (*c*).

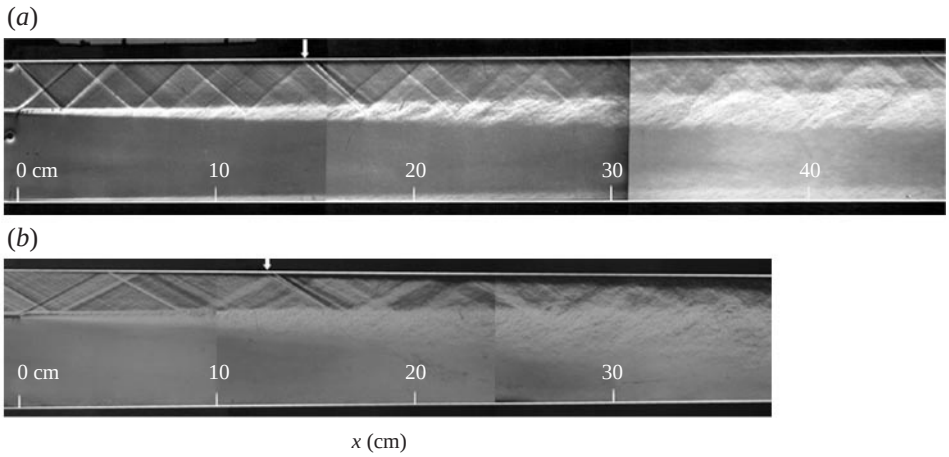

FIGURE 7. Schlieren images at $M_c = 0.25$ (*a*) and $M_c = 0.63$ (*b*). Arrows indicate top-window mismatch.

3. Results: compressibility effects

The focus of this section is a comprehensive planar velocity survey of the compressible mixing layer, parametrized by convective Mach number and viewing configuration. Most quantities are presented as vector or contour fields in order to best exploit the planar nature of the measurement. However, collapse of the side-view data into transverse profiles is also used to permit examination of large-ensemble statistics and comparison with previous studies. Ensemble averages of the planar data, omitted here for brevity, are available in Urban (1999).

3.1. *Side views*

Side-view measurements were obtained at all three compressibilities; they depict the transverse velocity gradient driving the turbulence, and outline the primary characteristics of the flow.

3.1.1. *Velocity fields*

Laboratory-frame instantaneous velocity fields for the three compressibility levels are presented in figure 8. As with all side-view results to follow, these fields consist of 25×25 non-overlapping interrogation regions, and derive from a single set of instantaneous particle images. The interrogation regions are 80 pixels (about 0.9 mm) square. In order to accentuate the transverse variations in velocity, only every second column of the measured vector field is depicted.

In the $M_c = 0.25$ case, the high velocity ratio (0.7) makes variations in the velocity field difficult to discern in the laboratory frame. Moderate angular undulations in the vectors are apparent, along with slight variations in the transverse velocity profile shapes.

The lab-frame view of the velocity data yields more information in the $M_c = 0.63$ and $M_c = 0.76$ cases, with their larger shear. In both of these cases, we observe considerable variation in the instantaneous profiles, with many realizations containing local extrema at varying transverse locations. Furthermore, considerable intermittency is evident at both interfaces, with near-free-stream velocity values persisting well into the turbulent region at certain streamwise locations. The spatial distribution of these events, on the order of 1–2 cm, is on the same order as the integral scale of the layer, or of the size of the large-scale turbulent structures; this suggests that interaction with the large-scale turbulence in the layer is the driving force for momentum exchange to and from entrained free-stream fluid. Angular variations in the compressible cases are also more marked than they were at $M_c = 0.25$, with clearly evident 'pinching' regions where the streamlines converge, either due to density variations or three-dimensional motion; both of the latter factors are expected to be more prevalent in the compressible layer. Both the intermittency and flow angle characteristics of the velocity field may be described using the present techniques; these are pursued in subsequent sections.

3.1.2. *Instantaneous streamlines*

To highlight the spatial variations in the velocity field, we provide instantaneous streamlines for the three cases in figure 8. The streamlines are obtained by integrating the Lagrangian paths of arbitrarily placed hypothetical fluid parcels in the experimentally measured instantaneous flow field. The result is a family of lines which are at all points tangent to the local velocity vector. Since the actual flow is turbulent, these instantaneous streamlines are *not* streaklines; that is, they do not depict the paths taken by fluid parcels in the actual flow in the time following the measurement.

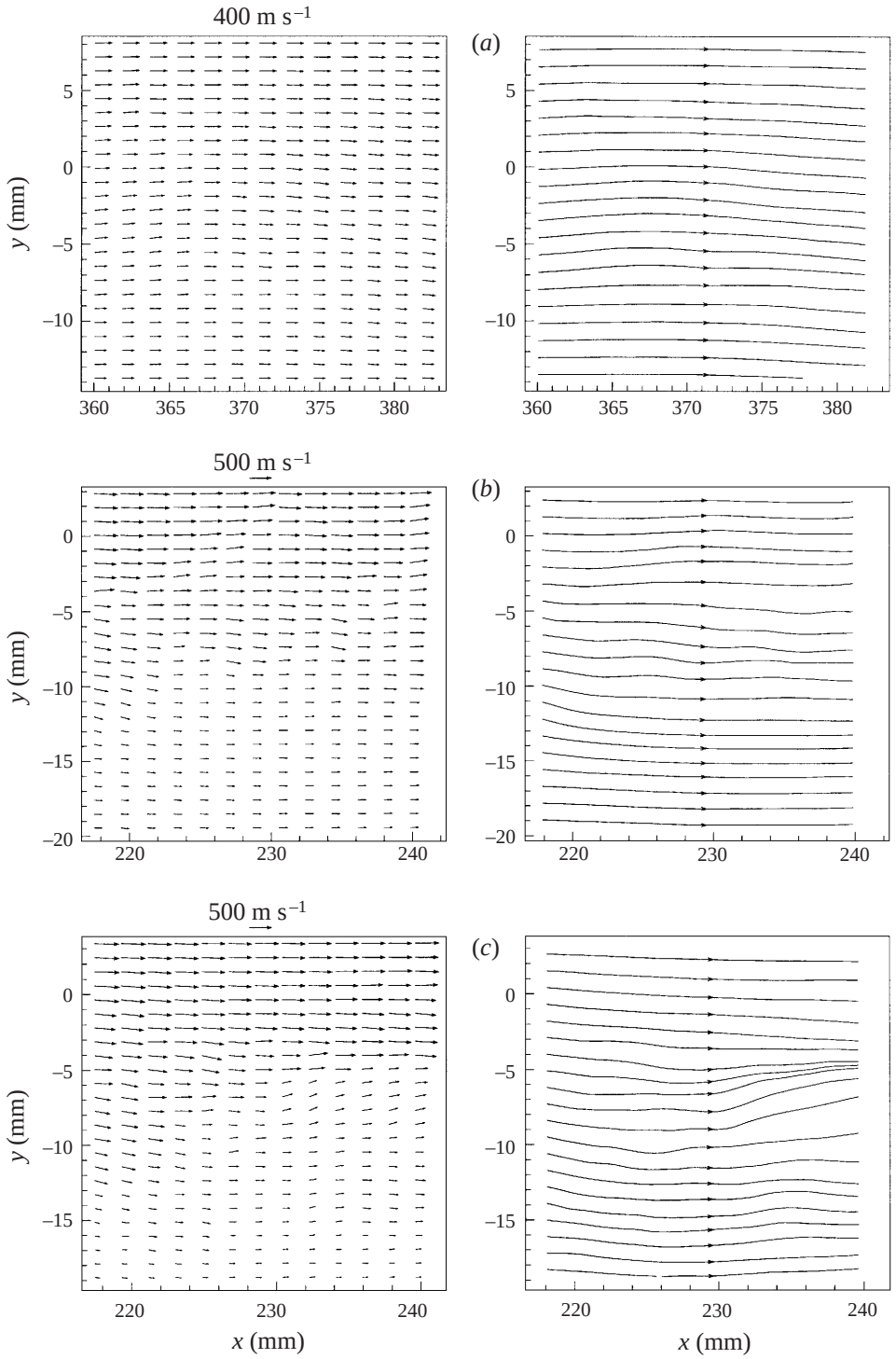

FIGURE 8. Side-view instantaneous velocity fields (left) and streamlines (right): (*a*) $M_c = 0.25$, (*b*) $M_c = 0.63$, and (*c*) $M_c = 0.76$.

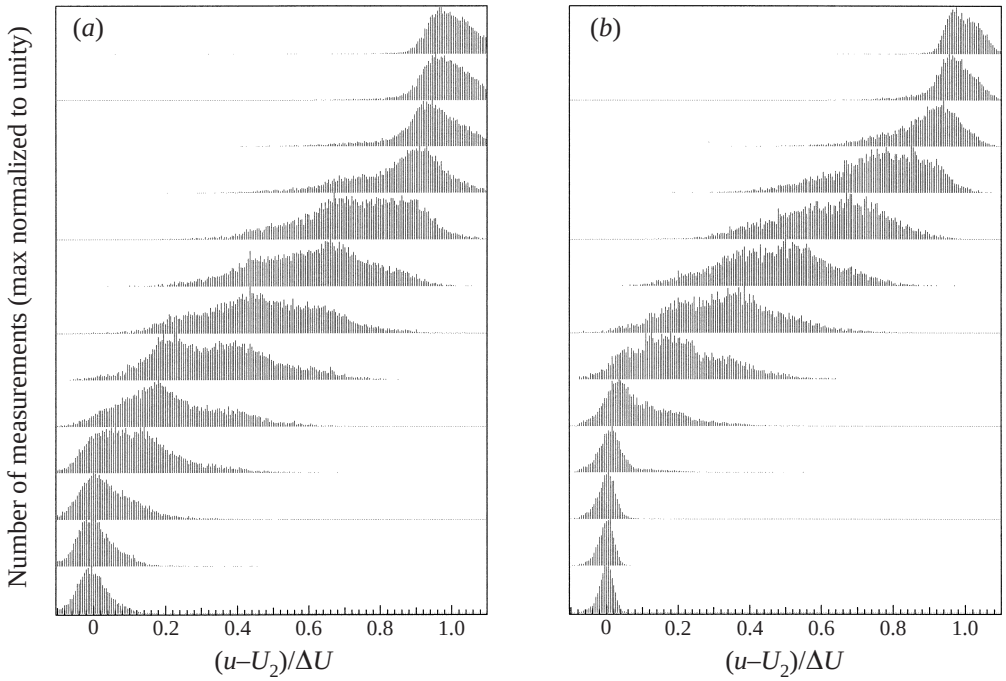

FIGURE 9. Side-view velocity PDFs: (*a*) $M_c = 0.25$ and (*b*) $M_c = 0.63$.

Nevertheless, they are useful to highlight the spatial characteristics of the measured velocity fields.

Figure 8 confirms the increases in transverse meandering with compressibility noted above, and also alerts us to regions of steep velocity gradients (i.e. rapid changes in streamline spacing) in the compressible cases.

3.1.3. *Velocity PDFs*

In order to characterize the intermittency at the free-stream interfaces, probability density functions (PDFs) of velocity are useful. Through comparison of PDFs obtained at varying transverse locations, it is possible to determine the spatial distribution of momentum exchange between incoming free-stream fluid and that already present in the mixing layer. The large-ensemble nature of the present measurements allows us to approximate the desired PDFs closely by appropriately normalized histograms, each typically representing 4000–10 000 independent measurements. Because the variance of the velocity distribution increases so much between the free streams and the centre of the layer, the true PDFs (i.e. area normalized to unity) have much larger peak heights at the free streams. Therefore, in order to facilitate presentation, we normalize each histogram in the transverse family to have the same peak height. Although this masks the characteristic that PDFs with larger variances (i.e. in the centre of the layer) have lower peak heights, it simplifies qualitative comparison of the histogram shapes and positions.

Histograms for the $M_c = 0.25$ and $M_c = 0.63$ cases studied are presented in figure 9; the results at $M_c = 0.76$ are substantially similar to those at $M_c = 0.63$ and are therefore omitted here. As expected, the variance of the PDFs (i.e. the velocity fluctuation u') increases as we move toward the centre of the layer for all cases. However, the increase in variance does not take the form of a simple widening of

a normal distribution; rather, due to the intermittency at the layer interfaces, the variance first increases through skewing of the distribution, with the peak relatively stationary at the free-stream value. On the low-speed side, this skewing eventually transforms to full-blown bimodality just below the layer centreline. The magnitude of this departure from the normal distribution is particularly apparent if we plot both the peaks (modes) and the means of the PDFs as a function of transverse location (figure 10). Several features are apparent from these plots. First, the skewness described above results in the PDF peaks lying closer to the free-stream velocity values than the corresponding means. Second, this effect is stronger on the low-speed side of the layer, where the free-stream peak (analogous to the pure-fluid delta function in a scalar PDF) persists further into the layer. This observation is tempered, however, by noting that the free-stream spikes in the velocity PDFs are generally smaller than those of mixture fraction PDFs. This is reasonable in view of the fact that the greatest amount of momentum is exchanged at the largest scales, and therefore happens quickly, while mixing takes place only at the bottom end of the turbulent cascade, when fluid motion has brought dissimilar fluid together at microscopic scales. Finally, we observe that the velocity PDFs exhibit a high degree of flatness near the centre of the layer, giving rise to ambiguity and scatter in the peak location.

3.1.4. *Velocity magnitude fields*

Since vector fields are difficult to interpret in a structural sense, it is beneficial to decompose the two-component velocity measurements into two scalars, magnitude and direction (flow angle), for structural analysis. In this section, we use velocity magnitude to study the distribution of momentum throughout the flow; in the next, we present measurements of flow angle.

Sample instantaneous velocity magnitude fields appear in figure 11. These maps permit identification of regions of high shear and fluid acceleration, and also provide structural patterns for comparison with scalar visualizations. In the incompressible case, each field tends to have a single region of steepest gradient which meanders through the central portion of the layer. At $M_c = 0.63$ and $M_c = 0.76$, however, there are generally multiple 'cliffs' (usually two) across the layer where velocity magnitude changes rapidly. Although their location meanders as well, there is generally one near each free-stream interface.

In any consideration of acceleration and deceleration in compressible flow, it is natural to inquire about the presence of shock and expansion waves in the velocity field. In a true free flow, however, the determination of an appropriate Mach number complicates the discussion of wave effects. As discussed in § 1, it becomes necessary to hypothesize a frame of reference in which the obstacle causing the disturbance is stationary, and to compute the relative Mach numbers of the streams in that frame.

However, the present flow is confined, and not truly free of lab-frame effects. Therefore, it is reasonable to examine the velocity field in the laboratory frame of reference for any evidence of wave activity. To this end, all the fields in figure 11 contain an indication of the lab-frame sonic velocity in the form of a discontinuity in the greyscale table. In each image, the contour colour reverts to white from dark grey at the point where the velocity is equal to the local speed of sound in the laboratory frame of reference. Note that it is possible to perform this mapping unambiguously without knowing the instantaneous temperature field since the temperature and velocity fields are linked by the energy equation; that is,

$$\frac{T_0}{T} = 1 + \frac{(\gamma - 1)}{2} M^2 \tag{3.1}$$

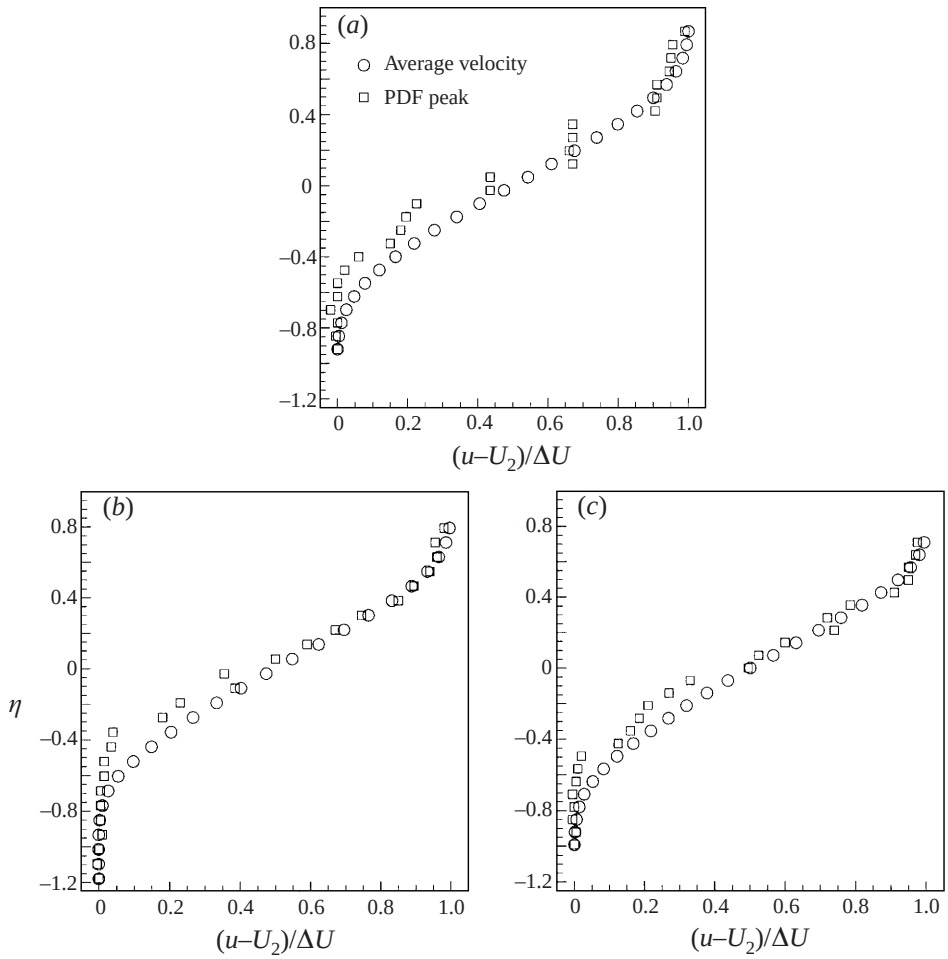

FIGURE 10. Trends in velocity PDF peaks: (*a*) $M_c = 0.25$, (*b*) $M_c = 0.63$ and (*c*) $M_c = 0.76$.

and

$$u = \sqrt{\gamma RT} \tag{3.2}$$

may be solved simultaneously to give $M = M(u)$ knowing only T_0; or more specifically to give u^*, where $M = 1$, without any assumption of an isentropic flow process:

$$u^* = \sqrt{2\frac{\gamma}{\gamma + 1}RT_0}. \tag{3.3}$$

Since the stagnation temperatures of the two free streams are similar, this analysis applies to fluids from either free stream. A small error arises in the $M_c = 0.76$ case, where the differing values of R and γ introduce a difference of about 12% in u^*.

The result of the analysis is that the lab-frame sonic line in the compressible cases seems frequently to coincide with the region of steep gradients lying closest to the low-speed interface. This implied sensitivity to lab-frame effects recalls the strong response of the layer to small, sub-boundary layer disturbances attached to the splitter tip (Island, Urban & Mungal 1998).

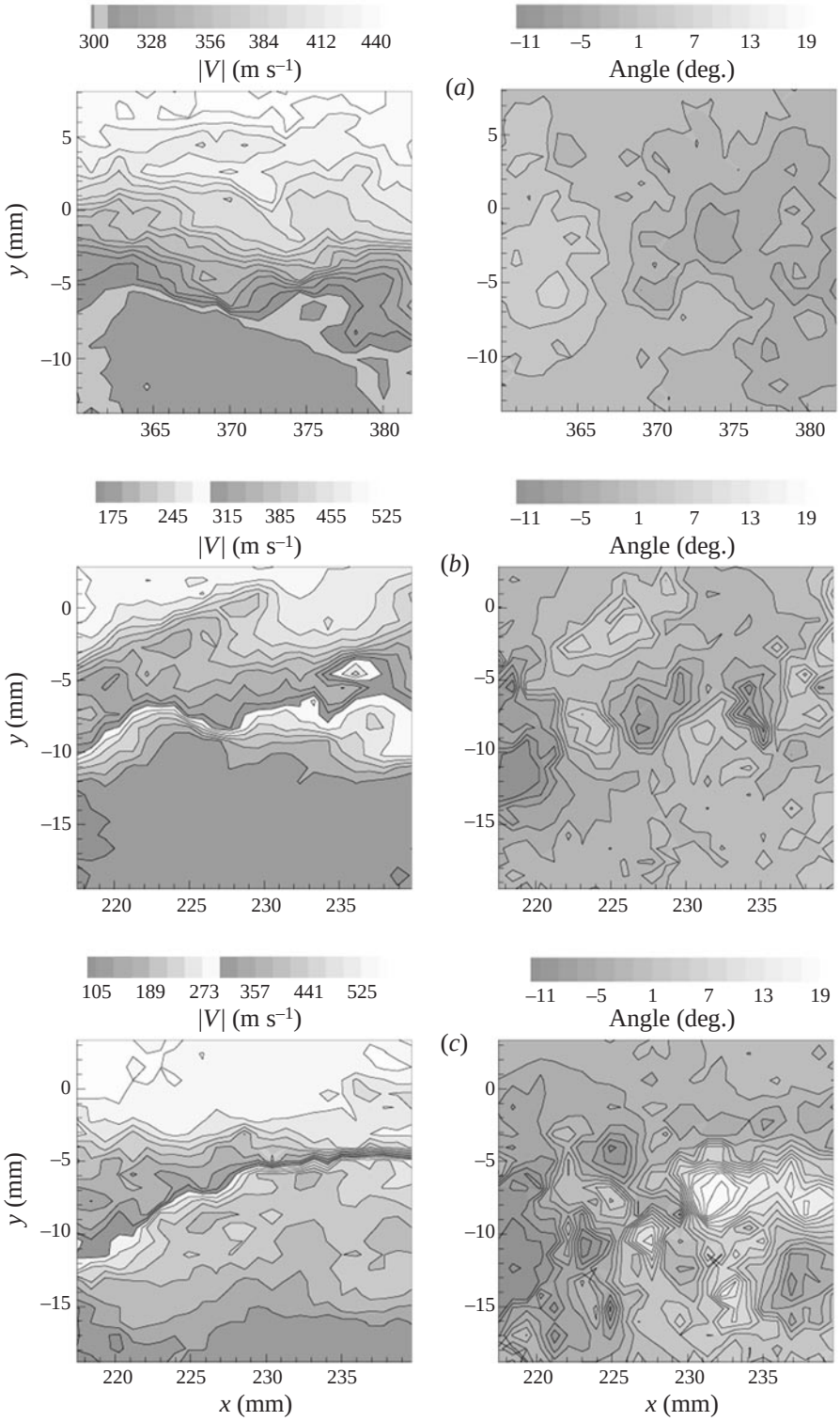

FIGURE 11. Side-view instantaneous velocity magnitude (left) and flow angle (right) fields: (*a*) $M_c = 0.25$, (*b*) $M_c = 0.63$, and (*c*) $M_c = 0.76$.

3.1.5. *Flow angle fields*

Motivated by the importance of wave-like instabilities in turbulent shear flows, we present two-dimensional flow angle fields in figure 11. The streamwise periodicity (approximately 1 cm) of the flow angle is evident from this figure, as is the fact that the bulk of the variation is confined to a relatively narrow central portion of the range between the extreme values. The absolute value of the variation intensity increases with compressibility, the standard deviation increasing from 1.5° at $M_c = 0.25$ to 2.3° and 3.3° at $M_c = 0.63$ and $M_c = 0.76$, respectively. The difference between the $M_c = 0.63$ and $M_c = 0.76$ cases is more pronounced for this quantity than for most others observed.

3.1.6. *Vorticity fields*

One of the primary inducements to perform planar velocity measurements is the potential to measure vorticity directly. Scalar visualization techniques, in addition to their useful role in mixing studies, are often extended to provide inferences regarding vorticity; that is, *scalar structure* is often held to be synonymous with *vortical structure*. Indeed, this belief is central to many of our basic notions of turbulence and its visualization; yet it can be highly misleading in unsteady (i.e. all turbulent) flows. An early warning on this topic was issued by Hama (1962), who numerically integrated streaklines for particles released in a laminar shear flow upon which a deterministic, periodic temporal fluctuation had been imposed. Although the lab-frame instantaneous streamlines for the flow were smoothly undulating, with no recirculation, the particles were seen to roll up into well-defined structures. The particle trajectories were very sensitive to initial conditions, with adjacently released particles reaching wildly different terminal points due to bifurcations in the trajectories. As a result, the streaklines were nothing like the instantaneous streamlines for this particular unsteady flow. Scalar patterns share the temporally and spatially integrated character of streaklines, and so are similarly ill-suited to identifying kinematic characteristics such as vorticity. Another drawback to the inference of vorticity from scalar fields is that scalar structures are defined by their interfaces, generally at one or both free streams. In regions where the scalar concentration varies slowly, we have no information regardless of the presence or absence of vorticity. Thus, the capability of planar velocimetry to deliver vorticity information on a regularly spaced grid, derived directly from the velocity field, is especially appealing.

Instantaneous spanwise vorticity fields for the three compressibilities are presented in figure 12. The figure also includes convective-frame velocity vectors: the isentropically calculated U_c for each case has been subtracted from the u component of velocity. The overall vorticity trend is negative (clockwise), since the principal velocity gradient is a positive $\partial u/\partial y$. Furthermore, as we would expect from the mean velocity profile, the vorticity is higher near the centre of the layer where the peak velocity gradient is found. However, at all compressibilities the instantaneous vorticity fields exhibit considerable variation within these constraints. In each case, the extreme values of the vorticity map lie in localized, blotchy patterns corresponding to a random distribution of very high measured velocity gradient. However, the distribution of vorticity contours at more moderate magnitudes does show variation with compressibility. In particular, the envelope described by the medium-vorticity contours for the $M_c = 0.25$ case resembles the large-scale structure familiar from incompressible scalar visualizations, extending to the free-stream interface in the 'roller' regions and contracting toward the centreline in the 'braid' regions. On the other hand, the corresponding levels at $M_c = 0.63$ and $M_c = 0.76$ exhibit prominent

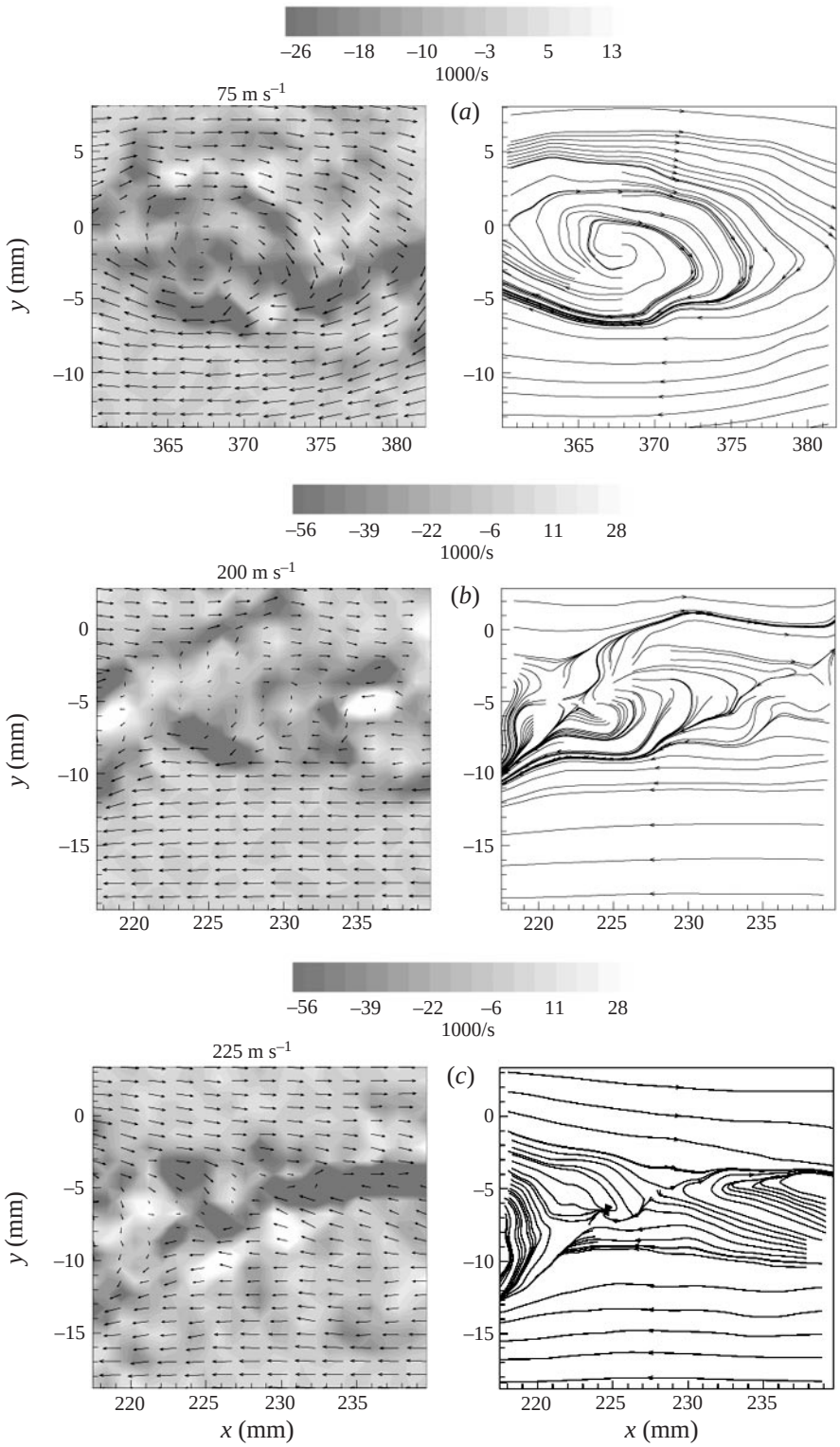

FIGURE 12. Side-view instantaneous vorticity (left) and streamlines (right): (*a*) $M_c = 0.25$, (*b*) $M_c = 0.63$, and (*c*) $M_c = 0.76$. Streamlines are derived from the velocity field in the frame of reference moving at U_c.

structural features *within* the envelope described by the diffuse, ill-organized scalar pattern. These features tend to take the form of thin streamwise sheets of vorticity which appear at varying transverse locations. The fact that these sheets span less of the layer than the incompressible rollers, and exhibit little transverse communication among themselves, suggests that fluid transport across the layer takes place in a halting fashion, proceeding rapidly across these regions of large gradients yet impaired in the relatively irrotational spaces between them. The resulting segregation manifests itself in the reduced transverse perturbation intensity and Reynolds stress observed in the compressible case, and thence to growth-rate suppression. The average number of sheets is two, corresponding to the two high-gradient regions observed in the velocity magnitude maps. In some cases, however, one sheet or three sheets are observed.

In the discussion above, we mentioned that the structural features of interest are superposed with sizable, randomly distributed small-scale vorticity perturbations. Instantaneous streamlines derived from the *shifted* velocity field (figure 12), as integral quantities, provide effective low-pass spatial filtering of the data, highlighting the vortical structure of the layer. In the incompressible case, the streamwise and transverse extents of the rollers are seen to be comparable, and their interface with the free stream to be regularly undulating. At the higher-compressibility conditions, the distinction between successive structures diminishes, and their shape flattens. This observation is consistent with results of covariance analysis of scalar structures (Elliott, Samimy & Arnette 1995; Messersmith & Dutton 1996). The free-stream interfaces are characterized by long, thin regions of steep velocity gradient corresponding to the sheets of vorticity described before. Another characteristic attending the decrease in coherence and roundness of the structures is the streamwise stretching of the region where u lies near U_c. In the incompressible case, the circularity of the instantaneous streamlines confines the (shifted-frame) zero-velocity singularities to small regions at the vortex cores. At higher M_c, $u = U_c$ along a streamwise locus of points in many of the realizations. As we see from the figures, when u is near U_c, the flow angle in the shifted frame is nearly vertical but highly sensitive to random sign fluctuations in u.

It should be noted that our observations on the vorticity maps are based upon a sampling of representative images. The incompressible vorticity field does not always display a clear roller–braid structure, while the thin-sheet structure occasionally degenerates to a more disorganized distribution of vorticity in the compressible case.

3.1.7. *Large-ensemble statistics*

In this section, we present transverse profiles of large-ensemble statistics based on the measured velocity fields. Convergence of the statistics is assured by forming large ensembles from the 25 columns of a large number (typically 300–400) of images. All statistics are displayed in similarity coordinates.

Normalized streamwise mean velocity profiles for the three compressibilities are presented in figure 13. The excellent collapse emphasizes the strong similarity of the layer across the compressibility range. In particular, the differences in character of the velocity magnitude fields are entirely obliterated in the mean, pointing up the utility of instantaneous diagnostics in isolating structural features.

A similar observation holds for the vorticity fields (figure 14). Although the absolute magnitudes of the vorticities for the three cases differed considerably, the values scale well with ΔU and b, and have similar profile shapes. Since the mean vorticity profile for the mixing layer corresponds to the mean velocity gradient profile $-\partial u/\partial y$, this measurement serves as validation for our vorticity measurement and calculation scheme. The profiles in figure 14 were obtained by streamwise and image-ensemble

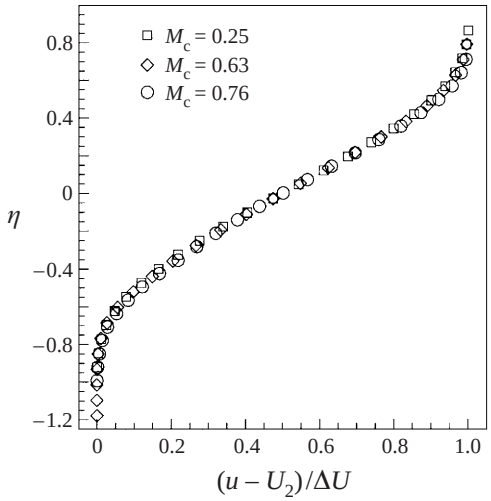

FIGURE 13. Mean profiles of streamwise velocity.

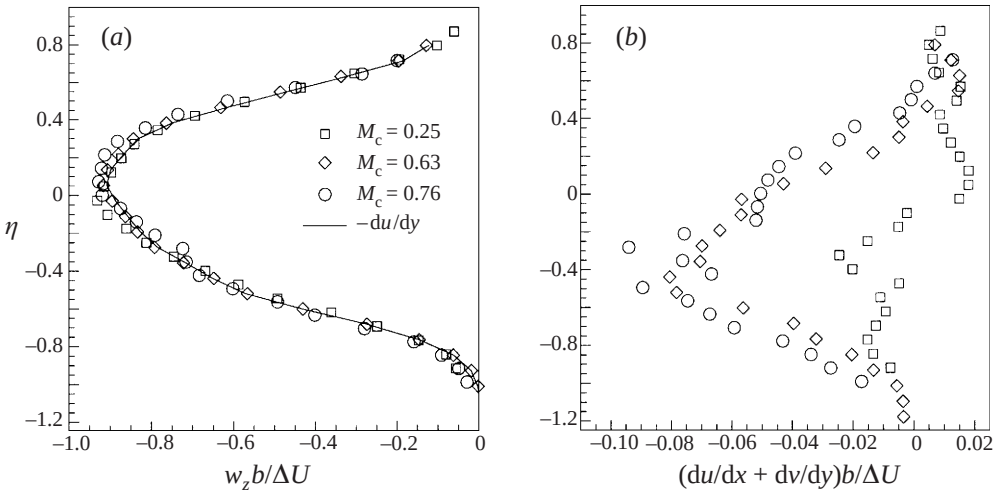

FIGURE 14. (*a*) Mean profiles of spanwise vorticity and (*b*) two-dimensional divergence.

averaging of instantaneous vorticity fields like those in figure 12, yet they collapse with compressibility onto the $-\partial u/\partial y$ curve indicated by the line.

In compressible flow, density variations cause Poisson's equation to break down, resulting in non-zero values for the divergence of the velocity field. With a planar measurement technique, two components of the divergence may be calculated: $\partial u/\partial x + \partial v/\partial y$. Since we expect the role of three-dimensionality to increase with compressibility, this quantity is only a crude indicator of the presence of compressible-flow phenomena. The roughness of this approximation is borne out by the scatter in its transverse profiles (figure 14). However, the two compressible cases do exhibit much higher peak values than the incompressible case; furthermore, these values lie near the transverse location of the sonic line, giving further evidence for the presence of strong recompressions in that zone.

The streamwise turbulence intensity (figure 15*a*) exhibits only a slight decrease

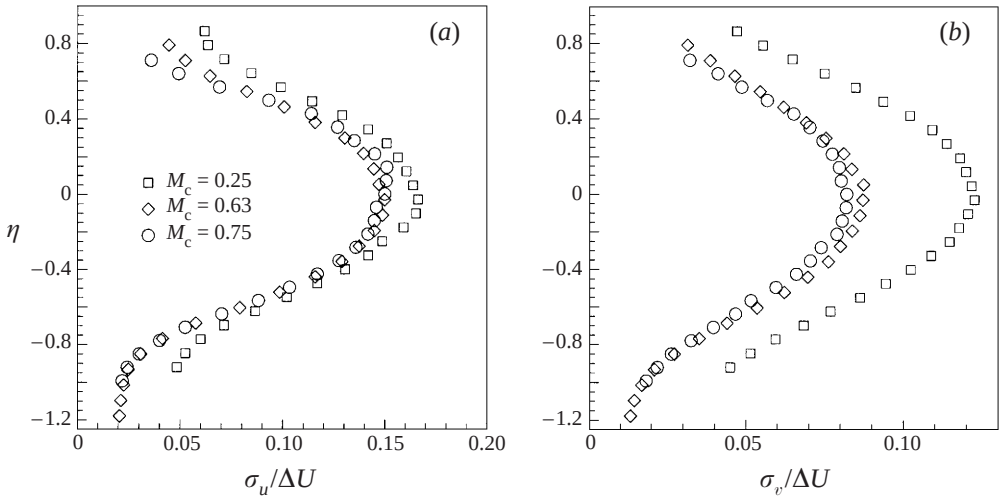

FIGURE 15. Mean profiles of (*a*) streamwise and (*b*) transverse velocity perturbations.

Case	$\sigma_u/\Delta U$	$\sigma_v/\Delta U$	$-\langle u'v'\rangle/\Delta U^2$
$M_c = 0.25$	0.166	0.122	0.0114
$M_c = 0.63$	0.150	0.088	0.0081
$M_c = 0.76$	0.151	0.082	0.0079

TABLE 2. Summary of peak turbulence statistics.

in its peak value across the compressibility range studied. This result is consistent both with pointwise measurements (e.g. Goebel & Dutton 1991) and direct numerical simulation (Freund 1997). In all cases, the perturbation peak occurs at the local mixing-layer centreline.

By contrast, the transverse turbulence intensity (figure 15*b*) is sharply reduced by compressibility, falling 28% between $M_c = 0.25$ and $M_c = 0.63$. However, the effect seems to saturate near that point, since the peak at $M_c = 0.76$ is only 7% lower. The peaks of σ_v, like those of σ_u, align with the local centreline. The observed behaviour of the transverse turbulence intensity agrees well with the numerical and experimental studies cited above.

A crucial validation of our technique and execution lies in the kinematic Reynolds stress profiles (figure 16*a*). These also agree well with previous measurements, and show the strong (29%) attenuating effect of compressibility. The peak lies near the centreline in all cases. All three primary turbulence quantities (σ_u, σ_v, and $\langle u'v'\rangle$) show similarity of profile, with the shape largely unaltered by compressibility. Trends in the peak values of the statistics are summarized in table 2.

Two secondary turbulence quantities, the perturbation asymmetry σ_u/σ_v and the Reynolds stress correlation coefficient $-\langle u'v'\rangle/\sigma_u\sigma_v$, are presented in figures 16(*b*) and 17. The former reflects the depression of transverse turbulence intensity (at roughly constant streamwise turbulence intensity) by moving farther from unity. The peak correlation coefficient is relatively insensitive to compressibility, and lies near 0.6. Both quantities agree well with the corresponding results of Goebel & Dutton (1991).

The Reynolds-stress results of this study are presented in the context of previous

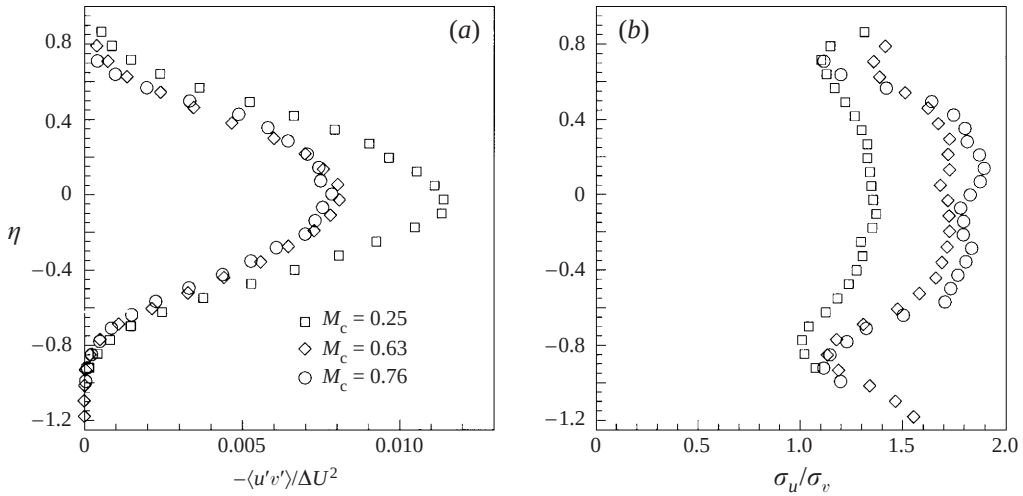

FIGURE 16. (*a*) Mean profiles of Reynolds stress and (*b*) perturbation asymmetry.

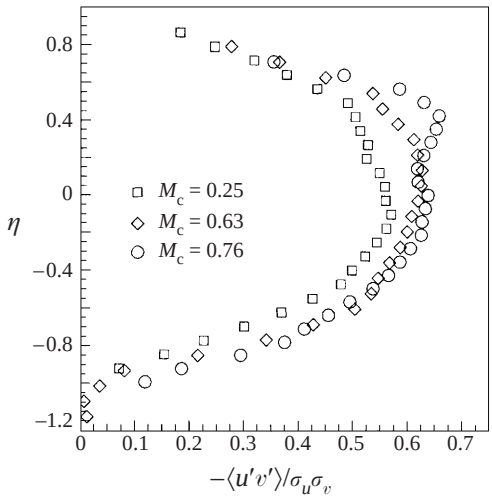

FIGURE 17. Mean profiles of Reynolds stress correlation coefficient.

(pointwise) measurements in figure 18. The figure shows a good match with the other work in both absolute magnitude and trend with compressibility, providing validation of the particles, imaging system, and analysis technique. Thus this work has produced, in a planar survey, turbulence statistics comparable to those resulting from the most rigorous pointwise studies; our spatial resolution (≈ 0.9 mm) is similar to that achieved by LDV. As described in § 1, LDV experiments have been performed with both atomized oil droplets and solid TiO_2 seed similar to that used in this work.

3.2. *Plan views*

Plan views of the mixing layer complement the side-view results by providing a third velocity component and by conveying spanwise variations in field quantities. Unlike the side view, with its strong transverse velocity gradient, the plan view possesses no mean condition driving spanwise variations. We idealize the initial conditions of the mixing layer as being two-dimensional, so any variation observed in the spanwise

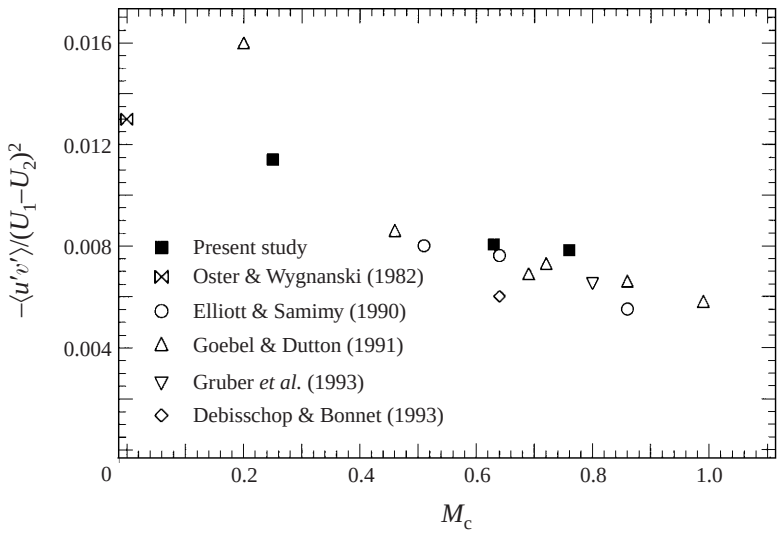

FIGURE 18. Peak Reynolds stress.

direction is understood to arise from perturbations and the associated response of the equations of motion. Scalar visualizations, however, have shown a clear increase in the role of three-dimensionality with compressibility. First, structures observed in side view, using both planar and especially spanwise-integrated diagnostics, become less organized (Clemens & Mungal 1995). Side-view organization is viewed as a proxy for two-dimensionality because the intersection or projection of a spanwise-uniform object (i.e. an eddy) with an (x, y)-plane at arbitrary z is unique; thus if side-view visualizations of many structures are similar, it is reasoned that they are two-dimensional. As spanwise variation increases, however, the side views become a composite image of random samplings of the variations, and hence appear disorganized. Plan-view visualizations (Island *et al.* 1996) have confirmed this interpretation, showing a progressive shift from predominantly spanwise structures at low compressibility, to oblique, inclined, or sometimes chevron-shaped structures at moderate compressibility, to a complete breakdown of spanwise structure at high compressibility. This is analogous to the result from linearized stability analysis that most-amplified stability modes possess obliquities to the z-axis which increase from zero at the incompressible limit to finite values at intermediate compressibilities, and which lose their meaning in the compressible limit when fully three-dimensional modes take over. In this section, we present plan-view PIV results and discussion. As before, compressibility effects are the primary concern; however, we also aim to assess the impact of the plan-view data on our interpretation of the side-view results already presented. Although PIV records an accurate projection of two components of velocity in the image plane (near the centre of the layer), the implicit assumptions we make in observing those two components in the absence of the third threaten to bias our interpretation unless we are mindful of the level of three-dimensional activity.

3.2.1. *Velocity fields*

Laboratory-frame velocity fields for the three compressibility levels are presented in figure 19. The field geometry is similar to that of the side-view cases, with 25×25 non-overlapping interrogation regions. As with all plan-view results to follow, these fields derive from the same particle images. The interrogation regions are 80 pixels

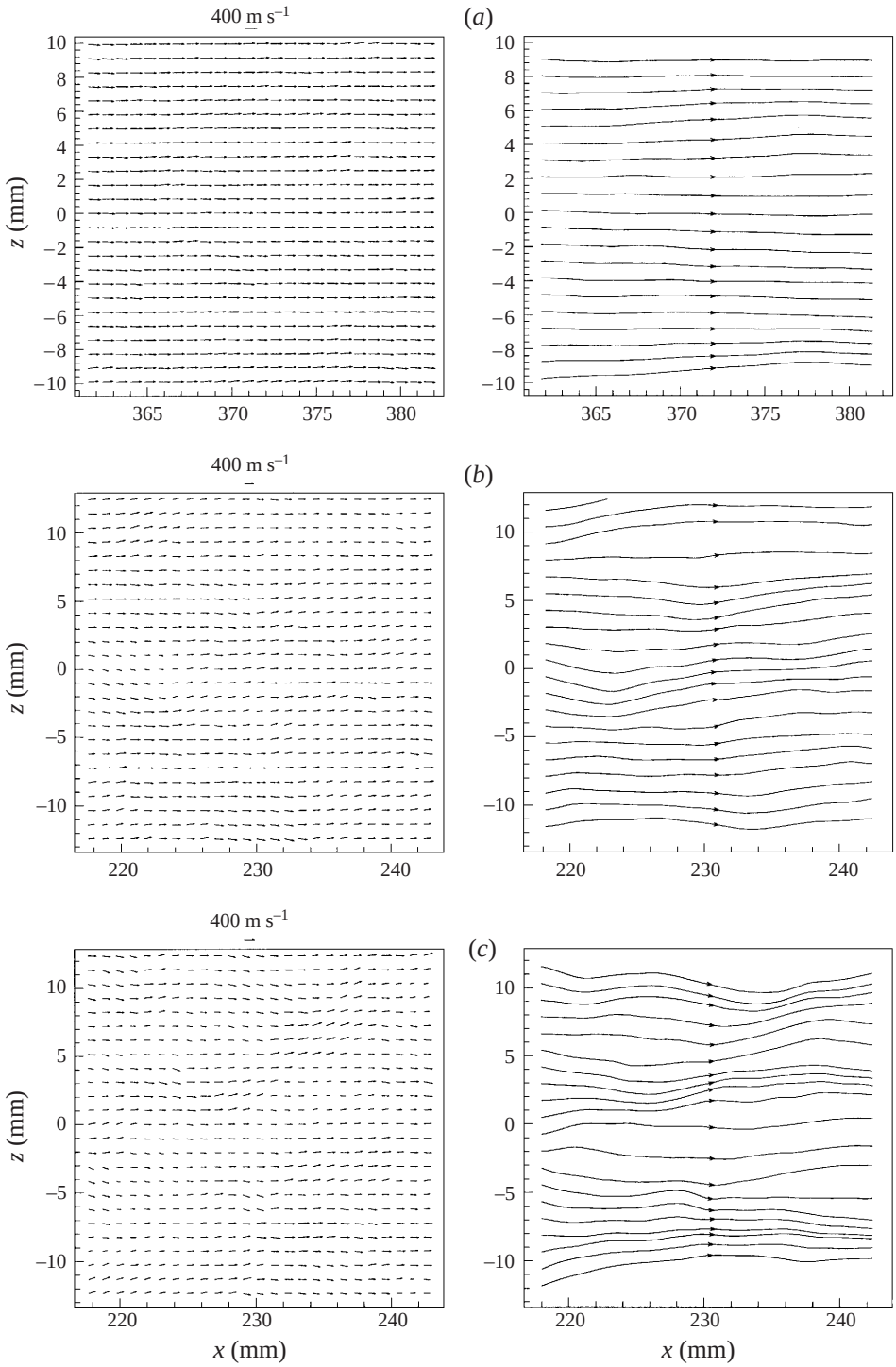

FIGURE 19. Plan-view instantaneous velocity fields (left) and streamlines (right): (*a*) $M_c = 0.25$, (*b*) $M_c = 0.63$, and (*c*) $M_c = 0.76$.

(0.9–1.0 mm) square. Due to the relative spanwise and streamwise uniformity of the plan-view velocity field, we dispense with the skipped-column strategy employed in the side-view case and instead present all vectors measured.

As compressibility increases, we notice that the primary change in the vector field lies in the amount of variation in the local flow angle. At $M_c = 0.25$, deviations from the principal flow direction are typically small. Some degree of organization is evident, however, in that the perturbed vectors tend to lie in obliquely inclined groups. Since the deviations tend to form and diminish at spatial scales smaller than the measurement volume, the nature of their development is difficult to discern. At $M_c = 0.63$ and $M_c = 0.76$, the meandering is more prominent both because of its increased amplitude and because the angular deviations define more clearly defined, mutually interacting structures. In both cases, but particularly at $M_c = 0.76$, the spatial patterns of perturbed vectors seem to appear in two forms. The first has a vortical appearance, where the vectors describe a smooth, double-inflected path as they diverge from the principal direction, pause at a peak divergence angle, and then relax back. The second pattern is a narrow, oblique line of perturbed vectors similar to that seen in the incompressible case. As we saw with the angular variations in side view, plan-view flow angle effects seem to exhibit more change with compressibility in the high-M_c range ($M_c = 0.63$ to $M_c = 0.76$) than do other quantities.

3.2.2. *Instantaneous streamlines*

The integrated effect of the velocity vector variations is revealed by the instantaneous streamlines, shown in figure 19. At $M_c = 0.25$, the relatively weak and localized meandering results in randomly disposed, mild bunching of the streamlines, with little spatial organization. Because of the increased magnitude and persistence of the variations, the compressible cases show structural features which are not only stronger but also exhibit longer-range organization, with longitudinally aligned bundles of streamlines persisting throughout the field of view.

3.2.3. *Velocity magnitude fields*

For the plan-view measurements, we again pursue the course of decomposing the velocity vector field into its constituent scalars, magnitude and direction. Sample instantaneous velocity magnitude fields, shown in figure 20, reveal a significant degree of variability in velocity magnitude not readily inferred from the vector plots. In all three cases, spatial magnitude fluctuations spanning the bounding (free-stream) velocities are present. Interestingly, the structure of these variations is seen to change little across the compressibility range examined. In all cases, the deviations are seen to lie in oblong 'islands' of fluid. In the plan view, interpretation of these results requires some care, since the instantaneous magnitude is calculated from only the two measured components of velocity, neither of which possesses mean variations in plan view. Variations may result from (*a*) momentum transfer to the transverse (unmeasured) component of velocity, (*b*) momentum transfer to adjacent fluid, or some combination of the two. The canonical incompressible roller structure provides a reference point, since it represents purely case (*a*). We would expect it to yield a banded plan-view magnitude field, since the leading and trailing edges of the roller are characterized by rising and falling fluid. But our magnitude maps lack this structure, even at $M_c = 0.25$. We conclude that there is significant spanwise momentum transfer, even though incompressible flow visualizations, with their banded appearance, only show spanwise scalar transfer in the braid region.

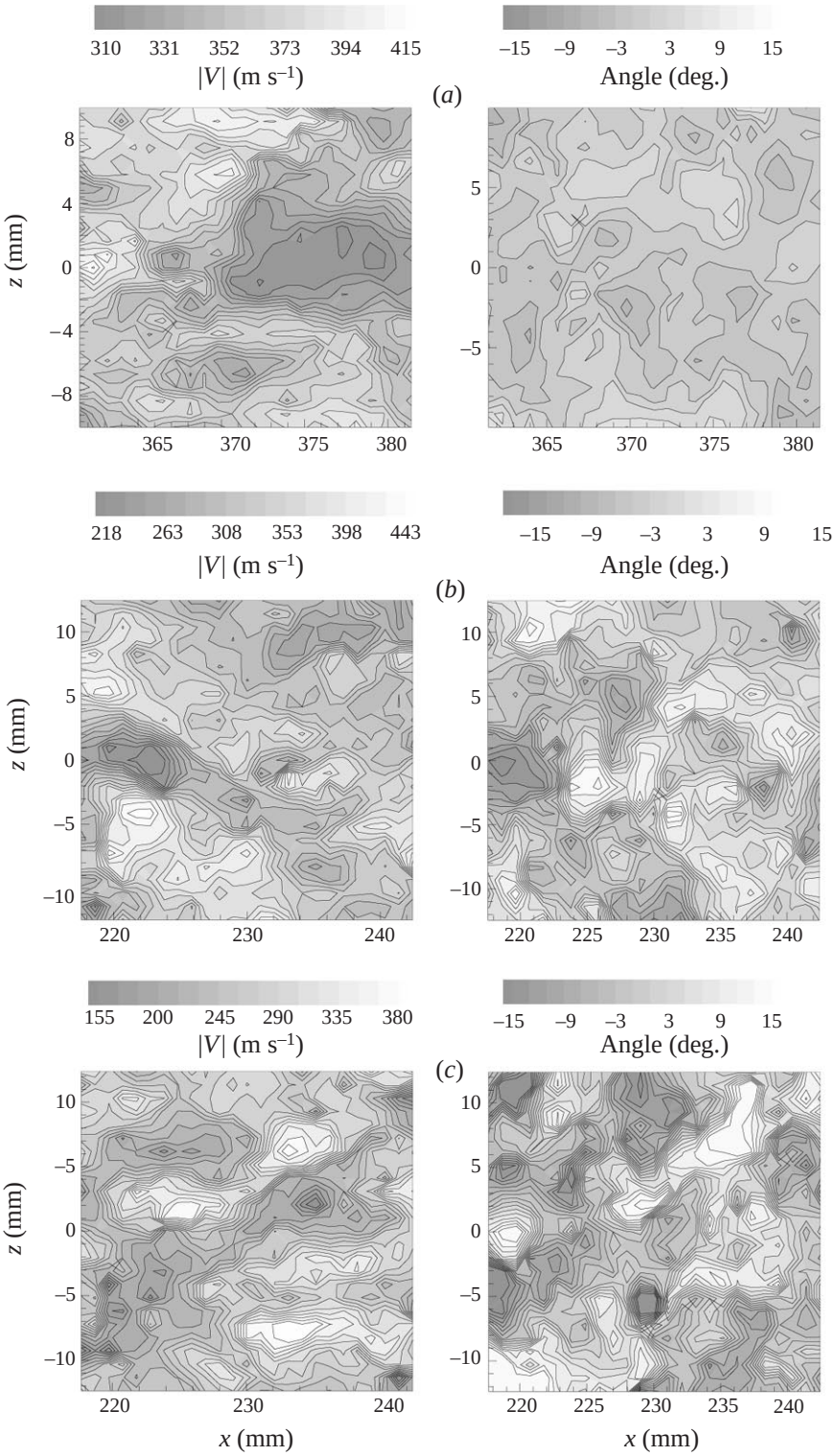

FIGURE 20. Plan-view instantaneous velocity magnitude (left) and flow angle (right) fields: (*a*) $M_c = 0.25$, (*b*) $M_c = 0.63$, and (*c*) $M_c = 0.76$.

3.2.4. *Flow angle fields*

To an even greater degree than the side-view data, the plan-view velocity measurements display marked changes in flow angle behaviour across the compressibility range. In this section, we characterize this by presenting and analysing the instantaneous flow angle as a scalar field quantity. Two-dimensional flow angle fields are presented in figure 20. The incompressible case is distinguished by mild variations with little spatial organization and only slight streamwise periodicity. At $M_c = 0.63$ and $M_c = 0.76$, however, the perturbation intensities increase and cycles of variation in the streamwise direction become apparent, albeit possessing only limited spanwise coherence. As in the side-view case, the bulk of the variation is confined to a relatively narrow central portion of the range between the extreme values. The absolute value of the variation intensity increases with compressibility, the standard deviation increasing from 1.6° at $M_c = 0.25$ to 2.6° and 3.6° at $M_c = 0.63$ and $M_c = 0.76$, respectively. These values are uniformly about 10% higher than the corresponding side-view results, with the same compressibility trend and similar spatial wavelength.

3.2.5. *Vorticity fields*

Instantaneous vorticity fields for the three compressibilities are presented in figure 21. Due to the absence of a driving velocity gradient, the vorticity fields are dominated by random high-frequency fluctuations. Aside from the diagonal regions of extreme vorticity arising from the oblique flow angle patterns observed in the vector fields, this view of the data presents few features of interest.

4. Conclusions

In this work, we have presented a comprehensive set of velocity measurements for the unperturbed mixing layer at convective Mach numbers ranging from 0.25 to 0.76. Taken together, the side- and plan-view instantaneous velocity fields enable us to supplement the well-known structural properties of the compressible mixing layer.

At all compressibilities, the u, v velocity field is characterized by a high degree of intermittency, with near-free-stream values of fluid velocity persisting well into the mixing layer. The resulting 'free-stream delta functions' in the velocity PDFs are analogous to the pure-fluid components of scalar PDFs, and tend to be stronger on the low-speed side of the layer. In compressible layers, the two-dimensional instantaneous velocity magnitude field often displays two or more lines of peak velocity gradient, in contrast to the single line present in the incompressible fields near the central point of the mean velocity profile. The peak gradient locus closest to the low-speed free stream coincides closely with the lab-frame sonic velocity, suggesting a sensitivity of the layer to stationary flow disturbances not expected in a true free shear layer. The angular variation intensity of the velocity field, in both side and plan view, increases with compressibility; the intensities in plan view are uniformly higher than those in side view. Velocity meandering in plan view usually takes the form of coherent regions of flow with similar flow angle, often oblong and inclined with respect to the streamwise direction.

The change from a roller–braid scalar structure at low compressibility to a more diffuse, disorganized nature at high compressibility is supported by direct measurements of the instantaneous vorticity field. However, high-frequency spatial variations in the instantaneous vorticity field superimposed on this basic structure are damped out over the integrated development of the scalar field. Instantaneous vorticity fields at high M_c reveal internal structure not visible in diffuse scalar visualizations. In

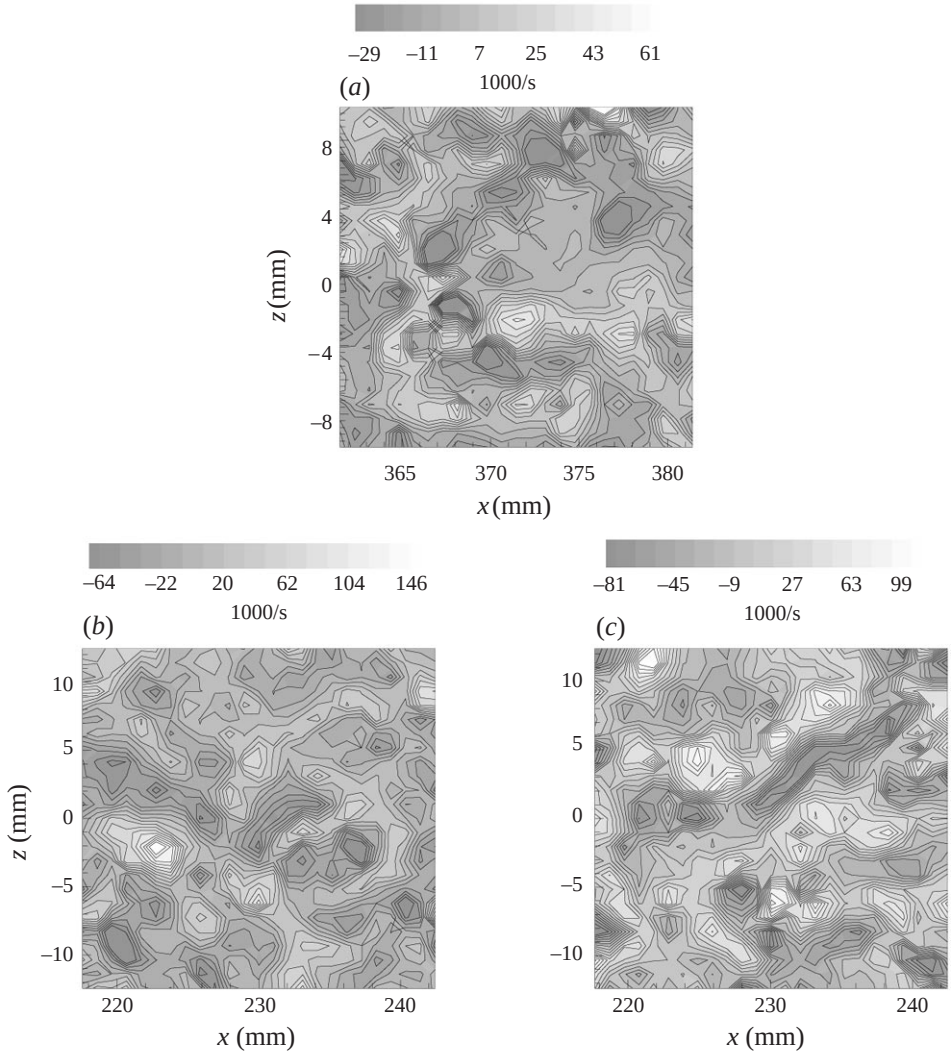

FIGURE 21. Plan-view instantaneous vorticity fields: (*a*) $M_c = 0.25$, (*b*) $M_c = 0.63$, and (*c*) $M_c = 0.76$.

particular, regions of high vorticity tend to organize into multiple, streamwise-aligned sheets, segregated from one another in the transverse direction. These sheets correspond to the multiple steep-gradient regions in the instantaneous velocity field and reflect the impairment of communication across the layer that ultimately results in growth-rate suppression. Instantaneous streamlines obtained by spatially integrating instantaneous velocity fields in a frame of reference travelling at a finite structure-convection velocity are similar to scalar visualizations. The shapes they describe are round and coherent at low M_c, and undergo a gradual flattening, inclination, and breakdown as compressibility increases. Ensemble-averaged, normalized transverse profiles of vorticity are highly insensitive to compressibility. Since the average vorticity profile is simply the average velocity gradient profile, this concordance validates our approach for obtaining vorticity data from the velocity measurements. A two-component approximation to the dilatation obtained from side-view velocity fields

provides a qualitative indication of the presence of compressibility effects, with increased activity at high M_c. The profiles peak near the lab-frame sonic line, again suggesting sensitivity to stationary disturbances.

Measurements of velocity fluctuations and Reynolds stress are in excellent agreement with simulations and other experiments. The peak streamwise turbulence intensity drops slightly with compressibility, while the transverse turbulence intensity and Reynolds stress are both strongly suppressed.

Collectively, these observations document compressibility-induced changes to the structure of the velocity field analogous to those previously observed in the scalar field. Global structural changes like those seen in scalar experiments are evident in the vorticity fields and instantaneous streamline patterns. Meanwhile, the idea that compressibility impairs mixing by interrupting transverse communication is supported by the observed behaviour of the velocity gradient and vorticity fields. This conclusion is also consonant with the sonic-eddy model, which predicts that the length scales of effective entrainment motions are limited to those which span velocity differences of the order of the local sound speed. The influence of stationary disturbances on the layer, as observed in experimental studies of growth-rate enhancement, is suggested by the apparent importance of the lab-frame sonic velocity in high-gradient regions. Finally, since the present measurements document the changes to turbulence quantities, they also support the connection between structure and kinematics that ultimately imposes growth-rate suppression upon compressible layers.

This work was sponsored by the National Science Foundation; additional support for W. D. U. was provided by the Air Force Office of Scientific Research AASERT program.

REFERENCES

Abramowich, G. N. 1963 *The Theory of Turbulent Jets*. MIT Press.

Barre, S., Quine, C. & Dussauge, J. P. 1994 Compressibility effects on the structure of supersonic mixing layers: Experimental results. *J. Fluid Mech.* **259**, 47–78.

Birch, S. F. & Eggers, J. M. 1972 A critical review of the experimental data for developed free turbulent shear layers. *Tech. Rep.* SP-321. NASA.

Bogdanoff, D. W. 1983 Compressibility effects in turbulent shear layers. *AIAA J.* **21**, 926–927.

Bowersox, R. D. W. & Schetz, J. A. 1995 Measurements of compressible turbulent flow structure in a supersonic mixing layer. *AIAA J.* **33**, 2101–2106.

Breidenthal, R. E. 1992 Sonic eddy–A model for compressible turbulence. *AIAA J.* **30**, 101–104.

Brown, G. L. 1974 The entrainment and large structure in turbulent mixing layers. In *Proc. 5th Australasian Conf. on Hydraulics and Fluid Mechanics*, pp. 352–359.

Brown, G. L. & Roshko, A. 1974 On density effects and large structure in turbulent mixing layers. *J. Fluid Mech.* **64**, 775–816.

Bryanston-Cross, P. J. & Epstein, A. 1990 The application of sub-micron particle visualisation for PIV (particle image velocimetry) at transonic and supersonic speeds. *Prog. Aerospace Sci.* **27**, 237–265.

Chang, C. T., Marek, C. J., Wey, C., Jones, R. A. & Smith, M. J. 1993 Turbulence measurement in a reacting and non-reacting shear layer at a high subsonic Mach number. *Ninth Symp. on Turbulent Shear Flows, Kyoto, Japan.*

Chinzei, N., Masuya, G., Komuro, T., Murakami, A. & Kudou, K. 1986 Spreading of two-stream supersonic turbulent mixing layers. *Phys. Fluids* **29**, 1345–1347.

Clemens, N. T. 1991 An experimental investigation of scalar mixing in supersonic turbulent shear layers. PhD thesis, Stanford University.

Clemens, N. T. & Mungal, M. G. 1995 Large-scale structure and entrainment in the supersonic mixing layer. *J. Fluid Mech.* **284**, 171–216.

Crisler, W., Krothapalli, A. & Lourenço, L. 1994 PIV investigation of high speed flow over a pitching airfoil. *AIAA Paper* 94-0533.

Crosswy, F. L. 1985 Particle size distributions of several commonly used seeding aerosols. In *NASA CP 2393: Wind Tunnel Seeding Systems for Laser Velocimeters* (ed. W. W. Hunter & C. E. Nichols), pp. 53–75.

Day, M. J., Reynolds, W. C. & Mansour, N. N. 1998 The structure of the compressible reacting mixing layer: Insights from linear stability analysis. *Phys. Fluids* **10**, 993–1007.

Debisschop, J. R. & Bonnet, J. P. 1993 Mean and fluctuating velocity measurements in supersonic mixing layers. In *Engineering Turbulence Modelling and Experiments 2* (ed. W. Rodi & F. Martelli), pp. 467–478. Elsevier.

Debisschop, J. R., Chambres, O. & Bonnet, J. P. 1994 Velocity field characteristics in supersonic mixing layers. *Expl Thermal Fluid Sci.* **9**, 147–155.

Dimotakis, P. E. 1991 On the convection velocity of turbulent structures in supersonic shear layers. *AIAA Paper* 91-1724.

Dimotakis, P. E. & Brown, G. L. 1976 The mixing layer at this Reynolds number: Large-structure dynamics and entrainment. *J. Fluid Mech.* **78**, 538–560.

Elliott, G. S. & Samimy, M. 1990 Compressibility effects in free shear layers. *Phys. Fluids* A **2**, 1231–1240.

Elliott, G. S., Samimy, M. & Arnette, G. S. 1995 The characteristics and evolution of large-scale structures in compressible mixing layers. *Phys. Fluids* **7**, 864–876.

Elliott, G. S., Samimy, M. & Arnette, S. A. 1994 A molecular filter based velocimetry technique for high speed flows. *Exps. Fluids* **18**, 107–118.

Freund, J. B. 1997 Compressibility effects in a turbulent annular mixing layer. PhD thesis, Stanford University

Glawe, D., Goss, L., Gogineni, S., Bowersox, R., Terry, W. & Dasgupta, S. 1996 Digital two-color PIV measurements in a Mach 2.8 boundary layer. *AIAA Paper* 96-2799.

Glawe, D. D. & Samimy, M. 1993 Dispersion of solid particles in compressible mixing layers. *J. Propulsion Power* **9**, 83–89.

Goebel, S. G. 1990 An experimental investigation of compressible turbulent mixing layers, PhD thesis, University of Illinois at Urbana-Champaign.

Goebel, S. G. & Dutton, J. C. 1990 Velocity measurements of compressible, turbulent mixing layers. *AIAA Paper* 90-0709.

Goebel, S. G. & Dutton, J. C. 1991 Experimental study of compressible turbulent mixing layers. *AIAA J.* **29**, 538–546.

Gropengiesser, H. 1969 On the stability of free shear layers in compressible flow (German translation). *Tech. Rep.* Technical Translation F-12, NASA.

Gruber, M. R., Messersmith, N. L. & Dutton, J. C. 1993 Three-dimensional velocity field in a compressible mixing layer. *AIAA J.* **31**, 2061–2067.

Hall, J. L., Dimotakis, P. E. & Rosemann, H. 1993 Experiments in nonreacting compressible shear layers. *AIAA J.* **31**, 2247–2254.

Hama, F. R. 1962 Streaklines in a perturbed shear flow. *Phys. Fluids* **5**, 644–650.

Ikawa, H. 1973 Turbulent mixing layer in supersonic flow. PhD thesis, California Institute of Technology.

Island, T. C. 1997 Quantitative scalar measurements and mixing enhancement in compressible shear layers. PhD thesis, Stanford University.

Island, T. C., Patrie, B. J., Mungal, M. G. & Hanson, R. K. 1996 Instantaneous three-dimensional flow visualization of a supersonic mixing layer. *Exps. Fluids* **20**, 249–256.

Island, T. C., Urban, W. D. & Mungal, M. G. 1998 Mixing enhancement in compressible shear layers via sub-boundary layer disturbances. *Phys. Fluids* **10**, 1008–1020.

Jackson, T. & Grosch, C. 1989 Inviscid spatial stability of a compressible mixing layer. *J. Fluid Mech.* **208**, 609.

Jackson, T. L. & Grosch, C. E. 1990 Absolute/convective instabilities and the convective Mach number in a compressible mixing layer. *Phys. Fluids* A **2**, 949–954.

Kompenhans, J. & Höcker, R. 1988 Application of particle image velocimetry to high speed flows. In *Particle Image Displacement Velocimetry*, pp. 67–84. von Karman Institute for Fluid Dynamics.

Krothapalli, A., Wishart, D. P. & Lourenço, L. M. 1994 Near field structure of a supersonic

jet: 'On-line' PIV study. In *Seventh Intl Symp. on Applications of Laser Techniques to Fluid Mechanics*, pp. 26.5.1–26.5.6.

Leep, L. J., Dutton, J. C. & Burr, R. F. 1993 Three-dimensional simulations of compressible mixing layers: Visualizations and statistical analysis. *AIAA J.* **31**, 2039–2046.

Lele, S. K. 1989 Direct numerical simulation of compressible free shear flows. *AIAA Paper* 89-0374.

Lessen, M., Fox, J. & Zien, H. 1966 Stability of the laminar mixing of two parallel streams with respect to supersonic disturbances. *J. Fluid Mech.* **25**, 737.

Melling, A. 1986 Seeding gas flows for laser anemometry. In *AGARD CP-399: Conference on Advanced Instrumentation for Aero Engine Components*, pp. 8.1–8.11.

Messersmith, N. L. & Dutton, J. C. 1996 Characteristic features of large structures in compressible mixing layers. *AIAA J.* **34**, 1814–1821.

Miller, M. F. 1994 An experimental investigation of the effect of compressibility on a turbulent reacting mixing layer. PhD thesis, Stanford University.

Molezzi, M. J. & Dutton, J. C. 1993 Application of particle image velocimetry in high speed separated flows. *AIAA J.* **31**, 438–446.

Nichols, C. E. 1985 Experiments with solid particle seeding. In *NASA CP 2393: Wind Tunnel Seeding Systems for Laser Velocimeters* (ed. W. W. Hunter & C. E. Nichols), pp. 77–84.

Olsen, M. G. 1999 Planar velocity measurements in an incompressible and a weakly compressible mixing layer. PhD thesis, University of Illinois at Urbana-Champaign.

Oster, D. & Wygnanski, I. 1982 The forced mixing layer between parallel streams. *J. Fluid Mech.* **123**, 91–130.

Papamoschou, D. 1992 Effect of three-dimensionality on compressible mixing. *J. Propulsion Power* **8**, 247–249.

Papamoschou, D. & Lele, S. K. 1993 Vortex-induced disturbance field in a compressible shear layer. *Phys. Fluids* A **5**, 1412–1419.

Papamoschou, D. & Roshko, A. 1988 The compressible turbulent shear layer: An experimental study. *J. Fluid Mech.* **197**, 453–477.

Patrick, W. P. 1985 Overview of solid particle LV seeding techniques used at UTRC. In *NASA CP 2393: Wind Tunnel Seeding Systems for Laser Velocimeters* (ed. W. W. Hunter & C. E. Nichols), pp. 105–113.

Raffel, M., Höfer, H., Kost, F., Willert, C. & Kompenhans, J. 1996 Experimental aspects of PIV measurements of transonic flow fields at a trailing edge model of a turbine blade. In *Eighth Intl Symp. on Applications of Laser Techniques to Fluid Mechanics*, pp. 28.1.1–28.1.10.

Ragab, S. A. & Sheen, S. 1990 Numerical simulation of a compressible mixing layer. *AIAA Paper* 90-1669.

Ragab, S. A. & Wu, J. L. 1989 Linear instabilities in two-dimensional compressible mixing layers. *Phys. Fluids* A **1**, 957–966.

Ross, C. B. 1993 Calibration of particle image velocimetry in a shock-containing supersonic flow. Master's thesis, Florida State University, Tallahassee.

Sabin, C. M. 1965 An analytical and experimental investigation of the plane, incompressible, turbulent free-shear layer with arbitrary velocity ratio and pressure gradient. *Trans. ASME* **87**, 421–428.

Samimy, M. & Abu-Hijleh, B. A. 1989 Performance of laser Doppler velocimeter with polydisperse seed particles in high-speed flows. *J. Propulsion* **5**, 21–25.

Soetrisno, M., Eherhardt, S., Riley, J. J. & McMurtry, P. 1989 A study of inviscid, supersonic mixing layers using a 2nd-order total variational diminishing scheme. *AIAA J.* **27**, 1770–1778.

Strykowski, P. J., Krothapalli, A. & Forliti, D. J. 1996 Counterflow thrust vectoring of supersonic jets. *AIAA Paper* 96-0115.

Urban, W. D. 1999 Planar velocity measurements in compressible mixing layers. PhD thesis, Stanford University.

Urban, W. D. & Mungal, M. G. 1997*a* Fluid and structure velocity measurements in compressible mixing layers. *ASME paper FED SM* 97-3155, Fluids Engineering Division Summer Meeting, Vancouver, BC.

Urban, W. D. & Mungal, M. G. 1997*b* Planar velocity measurements in compressible mixing layers. *AIAA Paper* 97-0757.

Urban, W. D. & Mungal, M. G. 1998 A PIV study of compressible shear layers. In *Ninth Intl Symp. on Applications of Laser Techniques to Fluid Mechanics*, pp. 17.1.1–17.1.8.

URBAN, W. D., WATANABE, S. & MUNGAL, M. G. 1998 Velocity field of the planar shear layer: Compressibility effects. *AIAA Paper* 98-0697.

VREMAN, A. W., SANDHAM, N. D. & LUO, K. H. 1996 Compressible mixing layer growth rate and turbulence characteristics. *J. Fluid Mech.* **320**, 235–258.

WANG, Q. & SQUIRES, K. D. 1996 Particle transport in a nonuniformly seeded mixing layer. *AIAA Paper* 96-0683.